

Supporting Information for

Compositional and Structural Insights into the Nature of the H-Cluster Precursor on HydF

Anna G. Scott, Robert K. Szilagyi, David W. Mulder, Michael W. Ratzloff, Amanda S. Byer, Paul W. King, William E. Broderick, Eric M. Shepard, Joan B. Broderick

Department of Chemistry and Biochemistry, Montana State University, Bozeman, MT 59717
Biosciences Center, National Renewable Energy Laboratory, Golden, CO 80401, USA

Table of Contents

1. Fourier-Transform Infrared Spectroscopic Results

Figure S1.1: Low temperature (13 K) FTIR spectra of HydF^{EG} 1

2. Electron Paramagnetic Spectroscopic Results

Figure S2.1: X-band EPR spectra of as-purified HydF^{EG} at 25 K and 500 μ W microwave power..... 2

Figure S2.2: X-band EPR spectra of dithionite reduced HydF^{EG} at 15 K and 500 μ W microwave power..... 3

Table S2.1: EPR spectroscopic properties of the [2Fe-2S]⁺ and [4Fe-4S]⁺ clusters associated with HydF^{EG} and HydF^{ΔEG}. 4

3. Computational Modeling and Structure Refinement

Figure S3.1: The experimental structure of [4Fe-4S] cluster and its inner sphere protein environment taken from the 2.8 Å resolution structure (PDB ID 5KH0) of HydF from *Thermosiphon melanesiensis* (Ref. ¹). 5

Figure S3.2: The excised [4Fe-4S] cluster with inner-sphere ligands including peptide bonds from adjacent amino acids justified by the presence of H-bonding and peptide dipoles with the [4Fe-4S] cluster. 5

Figure S3.3: Ionic fragment decomposition (A) and spin coupling schemes (B) considered. 5

Figure S3.4: Structural changes as a function of refinement steps for the [4Fe-4S] cluster model from Figure S3.2 calculated at ωB97X-D/SVP level and illustrated here for the ‘abab’ coupling (Figure S3.3B). 6

Table S3.1: Energy changes (ΔE^{SCF} in kJ mol⁻¹) as a function of refinement steps of the [4Fe-4S] cluster model from Figure S3.2 calculated at ωB97X-D/SVP level. 6

4. Calculated Vibrational Spectra for [2Fe] Precursors

Figure S4.1: Comparison of the performance of ωB97X-D functional using def2TZVP all-electron basis set (A) for Rauchfuss (YOBSEN with DTMA ligand, Ref. ²) and Pickett (no XRD structure with PDT ligand, Ref. ³) without employing scaled quantum chemical force field correction and (B) assignment of diatomic stretching vibrational modes calculated at the same level. 7

Figure S4.2: Graphical illustration of structural and energetic differences for coordination isomers of $[\text{Fe}_2(\text{DTMA})(\text{CO})_4(\text{CN})_2]^{2-}$ complex at $\omega\text{B97X-D/def2TZVP}$ level using X-ray structure YOBSEN (apical/apical isomer), Ref ² and WOLROE (apical/basal isomer), Ref ⁴	8
Figure S4.3: Comparison of optimized structure and diatomic stretching frequencies without a force field correction for crystallographically characterized isomers of $[\text{Fe}_2(\text{dithiolate})(\text{CO})_{5-6}(\text{CN})_{1-0}]^{1-0}$ complexes at $\omega\text{B97X-D/def2TZVP}$ level using X-ray structure CAZMAR (Ref. ⁵), and ODEDUW (Ref. ⁶).....	9
Table S4.1: Comparison of geometric structure, relative energies, and diatomic stretching frequencies without a force field correction for coordination isomers of $[\text{Fe}_2(\text{DTMA})(\text{CO})_4(\text{CN})_2]^{2-}$ complex at $\omega\text{B97X-D/def2TZVP}$ level using X-ray structure YOBSEN (apical/apical isomer), Ref ² and WOLROE (apical/basal isomer), Ref ⁴	8
Table S4.2: Compilation of optimized structures and diatomic stretching frequencies calculated at generalized graduate approximation (GGA, pure and hybrid), metaGGA, double-hybrid (DH) density functional and wave function (Ψ) level using def2TZVP basis set.	10

5. Development of Scaled Quantum Chemical Force Fields

Figure S5.1: Summary of scaled quantum chemical force fields from literature (Refs. 7-9) and our work.	11
Figure S5.2: Dependence of scaling and shifting factors developed for scaled quantum chemical force fields as a function of presence of implicit (A), both explicit counter ion and implicit solvent environment (B) and using a smaller yet reliable basis set (C) for electronic structure calculation of the [4Fe-4S] cluster models.	12

6. Geometric, Energetic, and Vibrational Analyses of Model A

Figure S6.1: Optimized structure (A, at $\omega\text{B97X-D/def2TZVP}$ level) for $[\text{Fe}^{(\text{I})}\text{Fe}^{(\text{I})}]^{2-}$ Model A , non-specific binding at an arbitrary protein binding pocket and (B) calculated intramolecular distances and scaled diatomic stretching frequencies in comparison to the experimental HydF ^{EG} bands.	13
---	----

7. Geometric, Energetic, and Vibrational Analyses of Model B

Figure S7.1: Optimized structures (A-C, at $\omega\text{B97X-D/def2TZVP}$ level) for $[\text{Fe}^{(\text{I})}\text{Fe}^{(\text{I})}]^{2-}$ Model B-Cys , loss of CO from Model A and $[\text{Fe}]_{\text{F}}$ cluster model binding via a protein derived cysteine ligand and (D) calculated intramolecular distances and scaled diatomic stretching frequencies in comparison to the experimental HydF ^{EG} bands.	14
--	----

Figure S7.2: Optimized structures (A-C, at $\omega\text{B97X-D/def2TZVP}$ level) for $[\text{Fe}^{(\text{I})}\text{Fe}^{(\text{I})}]^{2-}$ Model B-Glu/Asp , loss of CO from Model A and $[\text{Fe}]_{\text{F}}$ cluster model binding via a protein derived glutamate/aspartate ligand and (D) calculated intramolecular distances and scaled diatomic stretching frequencies in comparison to the experimental HydF ^{EG} bands.	15
---	----

8. Geometric, Energetic, and Vibrational Analyses of Model C

Figure S8.1: Optimized structures (A-E, at $\omega\text{B97X-D/def2TZVP}$ level) for $[\text{Fe}^{(\text{I})}\text{Fe}^{(\text{I})}]^{2-}$ Model C-Glu/Asp , loss of CO from Model A , $[\text{Fe}]_{\text{F}}$ cluster model binding via a bridging glutamate/aspartate ligand to a ‘unique Fe site’ (modeled by $[\text{Fe}^{3+}(\text{SH})_3]$) and (F) calculated intramolecular distances and scaled diatomic stretching frequencies in comparison to the experimental HydF ^{EG} bands.	16–18
--	-------

Figure S8.2: Optimized structures (at ω B97X-D/def2TZVP level) for reduced $[\text{Fe}^{(\text{I})}\text{Fe}^{(\text{I})}]^{2-}$ (A-B) and oxidized ($\text{Fe}^{(\text{I})}\text{Fe}^{(\text{II})}$) (C-D) **Model C-His**, loss of CO from **Model A**, $[\text{Fe}]_F$ cluster model binding via a bridging histidine ligand to a ‘unique Fe site’ (modeled by $[\text{Fe}^{3+}(\text{SH})_3]$) and (E) calculated intramolecular distances and scaled diatomic stretching frequencies in comparison to the experimental HydF^{EG} bands. 18

9. Geometric, Energetic, and Vibrational Analyses of Model D

Figure S9.1: Optimized structures (at ω B97X-D/def2TZVP level) for oxidized $[\text{Fe}^{(\text{II})}\text{Fe}^{(\text{II})}]$ (A: X-ray B: calculated), one $[\text{Fe}^{(\text{I})}\text{Fe}^{(\text{II})}]^-$ (C), and two-electron reduced $[\text{Fe}^{(\text{I})}\text{Fe}^{(\text{I})}]$ (D) **Model D-Cys**, $[\text{Fe}]_F$ cluster model binding via a protein derived cysteine ligand and (E) calculated intramolecular distances and scaled diatomic stretching frequencies in comparison to the experimental HydF^{EG} and TABGEJ (Ref. ¹⁰) bands. 19

Figure S9.2: Optimized structures (at ω B97X-D/def2TZVP level) for oxidized $[\text{Fe}^{(\text{II})}\text{Fe}^{(\text{II})}]$ (A: X-ray B: calculated) and reduced $[\text{Fe}^{(\text{I})}\text{Fe}^{(\text{II})}]^-$ (C) **Model D-Glu/Asp**, $[\text{Fe}]_F$ cluster model binding via a protein derived glutamate/aspartate ligand and (D) calculated intramolecular distances and scaled diatomic stretching frequencies (in comparison to the experimental HydF^{EG} and TABGEJ (Ref. ¹⁰) bands. 20

Figure S9.3: Optimized structures (at ω B97X-D/def2TZVP level) for oxidized $[\text{Fe}^{(\text{II})}\text{Fe}^{(\text{II})}]$ (A) and reduced $[\text{Fe}^{(\text{I})}\text{Fe}^{(\text{II})}]^-$ (B-D) **Model D-Glu/Asp+DTMA** (fused structure of TABGEJ and YOBSEN complexes), $[\text{Fe}]_F$ cluster model binding via a protein derived glutamate/aspartate ligand and (F) calculated intramolecular distances and scaled diatomic stretching frequencies in comparison to the experimental HydF^{EG} bands. 21

10. Geometric, Energetic, and Vibrational Analyses of Model E

Figure S10.1: Optimized structures (at ω B97X-D/def2TZVP level) for oxidized $[\text{Fe}^{3+}] \times [\text{Fe}^{(\text{I})}\text{Fe}^{(\text{I})}]^{2-}$ (A-D) **Model E**, $[\text{Fe}]_F$ cluster model binding via a bridging cyanide ligand to a ‘unique Fe site’ (modeled by $[\text{Fe}^{3+}(\text{SH})_3]$) and (E) calculated intramolecular distances and scaled diatomic stretching frequencies in comparison to the experimental HydF^{EG} bands. 22

Figure S10.2: Optimized structures (at ω B97X-D/def2TZVP level) for reduced $[\text{Fe}^{2+}] \times [\text{Fe}^{(\text{I})}\text{Fe}^{(\text{I})}]^{2-}$ (A-B) **Model E**, $[\text{Fe}]_F$ cluster model binding via a bridging cyanide ligand to a ‘unique Fe site’ (modeled by $[\text{Fe}^{2+}(\text{SH})_3]^-$) and (C) calculated intramolecular distances and scaled diatomic stretching frequencies in comparison to the experimental HydF^{EG} bands and the one-electron oxidized form. 23

11. Geometric, Energetic, and Vibrational Analyses of Model F

Figure S11.1: Optimized structures (at ω B97X-D/SVP level) for oxidized, vicinal, *cis* $(\text{Cys})_2[2\text{Fe}-2\text{S}] \times [\text{Fe}^{(\text{I})}\text{Fe}^{(\text{I})}]^{2-}$ (A-B) **Model F**, $[\text{Fe}]_F$ cluster model binding via a bridging cyanide ligand in two arrangements from HydA with frozen backbone atoms. A water molecule completes the distal Fe coordination environment of the $[2\text{Fe}-2\text{S}]$ cluster. Atomic spin density contour plots at $0.003 e^- \text{\AA}^{-3}$ contour level (C-D). Calculated intramolecular distances and scaled diatomic stretching frequencies (E) in comparison to the experimental HydF^{EG} bands. 24

Figure S11.2: Optimized structures (at ω B97X-D/SVP level) for reduced vicinal, *cis* $(\text{Cys})_2[2\text{Fe}-2\text{S}]^- \times [\text{Fe}^{(\text{I})}\text{Fe}^{(\text{I})}]^{2-}$ (A-B) **Model F**, $[\text{Fe}]_F$ cluster model binding via a bridging cyanide ligand in two arrangements from HydA with frozen backbone atoms. A water molecule completes the distal Fe coordination environment of the $[2\text{Fe}-2\text{S}]$ cluster. Atomic spin density contour plots at $0.003 e^- \text{\AA}^{-3}$ contour level (C-D). Calculated intramolecular distances and scaled diatomic stretching frequencies (E) in comparison to the experimental HydF^{EG} bands. 25

- Figure S11.3:** Optimized structures (at ω B97X-D/SVP level) for oxidized, vicinal, *cis* (Cys)₂[2Fe-2S] \times [Fe^(I)Fe^(I)]²⁻ (A-B) **Model F**, [2Fe]_F cluster model binding *via* a bridging cyanide ligand in two arrangements from HydA without any constraints on atomic positions. A water molecule completes the distal Fe coordination environment of the [2Fe-2S] cluster. Atomic spin density contour plots at 0.003 $e^- \text{ \AA}^{-3}$ contour level (C-D). Calculated intramolecular distances and scaled diatomic stretching frequencies (E) in comparison to the experimental HydF^{EG} bands.....26
- Figure S11.4:** Optimized structures (at ω B97X-D/SVP level) for reduced vicinal, *cis* (Cys)₂[2Fe-2S] \times [Fe^(I)Fe^(I)]²⁻ (A-B) **Model F**, [2Fe]_F cluster model binding *via* a bridging cyanide ligand in two arrangements from HydA without any constraints on atomic positions. A water molecule completes the distal Fe coordination environment of the [2Fe-2S] cluster. Atomic spin density contour plots at 0.003 $e^- \text{ \AA}^{-3}$ contour level (C-D). Calculated intramolecular distances and scaled diatomic stretching frequencies (E) in comparison to the experimental HydF^{EG} bands.....27
- Figure S11.5:** Optimized structures (at ω B97X-D/SVP level) for oxidized, geminal (Cys)₂[2Fe-2S] \times [Fe^(I)Fe^(I)]²⁻ (A-B) **Model F**, [2Fe]_F cluster model binding *via* a bridging cyanide ligand in two arrangements from HydA without any constraints on atomic positions. Atomic spin density contour plots at 0.003 $e^- \text{ \AA}^{-3}$ contour level (C-D). Calculated intramolecular distances and scaled diatomic stretching frequencies (E) in comparison to the experimental HydF^{EG} bands.....28
- Figure S11.6:** Optimized structures (at ω B97X-D/SVP level) for reduced geminal (Cys)₂[2Fe-2S] \times [Fe^(I)Fe^(I)]²⁻ (A-B) **Model F**, [2Fe]_F cluster model binding *via* a bridging cyanide ligand in two arrangements from HydA without any constraints on atomic positions. A water molecule completes the distal Fe coordination environment of the [2Fe-2S] cluster. Atomic spin density contour plots at 0.003 $e^- \text{ \AA}^{-3}$ contour level (C-D). Calculated intramolecular distances and scaled diatomic stretching frequencies (E) in comparison to the experimental HydF^{EG} bands.....29
- Figure S11.7:** Optimized structures (at ω B97X-D/SVP level) for oxidized, (Cys)₃[2Fe-2S] \times [Fe^(I)Fe^(I)]²⁻ (A-B) **Model F**, [2Fe]_F cluster model binding *via* a bridging cyanide ligand in two arrangements from HydA without any constraints on atomic positions. Atomic spin density contour plots at 0.003 $e^- \text{ \AA}^{-3}$ contour level (C-D). Calculated intramolecular distances and scaled diatomic stretching frequencies (E) in comparison to the experimental HydF^{EG} bands.....30
- Figure S11.8:** Optimized structures (at ω B97X-D/SVP level) for reduced (Cys)₃[2Fe-2S] \times [Fe^(I)Fe^(I)]²⁻ (A-B) **Model F**, [2Fe]_F cluster model binding *via* a bridging cyanide ligand in two arrangements from HydA without any constraints on atomic positions. Atomic spin density contour plots at 0.003 $e^- \text{ \AA}^{-3}$ contour level (C-D). Calculated intramolecular distances and scaled diatomic stretching frequencies (E) in comparison to the experimental HydF^{EG} bands.....31

12. Geometric, Energetic, and Vibrational Analyses of Model G

- Figure S12.1:** Fully optimized *in vacuo* structures (at ω B97X-D/SVP level) for [4Fe-4S]²⁺ \times [Fe^(I)Fe^(I)]²⁻ (A-D) **Model G**, [2Fe]_F cluster model binding *via* a bridging cyanide ligand to an oxidized [4Fe-4S] cluster and (E) calculated intramolecular distances and scaled diatomic stretching frequencies in comparison to the experimental HydF^{EG} bands.....32
- Figure S12.2:** Partially optimized *in vacuo* structures (at ω B97X-D/SVP level) with constrained backbone atomic positions as in holo-HydA structure (3C8Y) for [4Fe-4S]²⁺ \times [Fe^(I)Fe^(I)]²⁻ (A-B) **Model G**, [2Fe]_F cluster model binding *via* a bridging cyanide ligand to an oxidized [4Fe-4S] cluster, (C-D) atomic spin density distribution plots (at 0.003 $e^-/\text{\AA}^3$ contour level), and (E) calculated intramolecular distances and scaled diatomic stretching frequencies in comparison to the experimental HydF^{EG} bands (relative energies are given to the lowest energy fully optimized structure).....33

Figure S12.3: Partially optimized <i>in proteo</i> structures (at ω B97X-D/SVP level) with constrained backbone atomic positions as in holo-HydA structure (3C8Y) and in the presence of three neutralizing methylammonium counter-ions for $[4\text{Fe}-4\text{S}]^{2+} \times [\text{Fe}^{(\text{I})}\text{Fe}^{(\text{I})}]^{2-}$ (A-B) Model G , $[2\text{Fe}]_{\text{F}}$ cluster model binding <i>via</i> a bridging cyanide ligand to an oxidized $[4\text{Fe}-4\text{S}]$ cluster, (C-D) atomic spin density distribution plots (at $0.003 \text{ e}^{-}/\text{\AA}^3$ contour level), and (E) calculated intramolecular distances and scaled diatomic stretching frequencies in comparison to the experimental HydF ^{EG} bands.	34
Figure S12.4: Partially optimized <i>in proteo</i> structures (at ω B97X-D/SVP level) with constrained backbone atomic positions as in holo-HydA structure (3C8Y) for $[4\text{Fe}-4\text{S}]^{1+} \times [\text{Fe}^{(\text{II})}\text{Fe}^{(\text{I})}]^{-}$ in open shell singlet (A) and spin-polarized triplet (B) states of Model G , oxidized $[2\text{Fe}]_{\text{F}}$ cluster model binding <i>via</i> a bridging cyanide ligand to a reduced $[4\text{Fe}-4\text{S}]$ cluster, (C-D) atomic spin density distribution plots (at $0.003 \text{ e}^{-}/\text{\AA}^3$ contour level), and (E) calculated intramolecular distances and scaled diatomic stretching frequencies in comparison to the experimental HydF ^{EG} bands.	35
Figure S12.5: Partially optimized <i>in proteo</i> structures (at ω B97X-D/SVP level) with constrained backbone atomic positions as in holo-HydA structure (3C8Y) for $[4\text{Fe}-4\text{S}]^{2+} \times [\text{Fe}^{(\text{II})}\text{Fe}^{(\text{I})}]^{-}$ in spin-polarized doublet state (A-B) of Model G , oxidized $[2\text{Fe}]_{\text{F}}$ cluster model binding <i>via</i> a bridging cyanide ligand to an oxidized $[4\text{Fe}-4\text{S}]$ cluster, (C-D) atomic spin density distribution plots (at $0.003 \text{ e}^{-}/\text{\AA}^3$ contour level), and (E) calculated intramolecular distances and scaled diatomic stretching frequencies in comparison to the experimental HydF ^{EG} bands.	36
Figure S12.6: Partially optimized <i>in proteo</i> structures (at ω B97X-D/SVP level) with constrained backbone atomic positions as in holo-HydA structure (3C8Y) for $[4\text{Fe}-4\text{S}]^{1+} \times [\text{Fe}^{(\text{I})}\text{Fe}^{(\text{I})}]^{2-}$ in spin-polarized doublet state (A-B) of Model G , reduced $[2\text{Fe}]_{\text{F}}$ cluster model binding <i>via</i> a bridging cyanide ligand to an reduced $[4\text{Fe}-4\text{S}]$ cluster, (C-D) atomic spin density distribution plots (at $0.003 \text{ e}^{-}/\text{\AA}^3$ contour level), and (E) calculated intramolecular distances and scaled diatomic stretching frequencies in comparison to the experimental HydF ^{EG} bands.	37
Figure S12.7: Partially optimized <i>in proteo</i> structures (at ω B97X-D/SVP level) with constrained backbone atomic positions as in holo-HydA structure (3C8Y) and in the presence of three neutralizing methylammonium counter-ions for $[4\text{Fe}-4\text{S}]^{1+} \times [\text{Fe}^{(\text{I})}\text{Fe}^{(\text{I})}]^{2-}$ (A-B) Model G , reduced $[2\text{Fe}]_{\text{F}}$ cluster model binding <i>via</i> a bridging cyanide ligand to a reduced $[4\text{Fe}-4\text{S}]$ cluster, (C-D) atomic spin density distribution plots (at $0.003 \text{ e}^{-}/\text{\AA}^3$ contour level), and (E) calculated intramolecular distances and scaled diatomic stretching frequencies in comparison to the experimental HydF ^{EG} bands.	38
Figure S12.8: Comparison of partially optimized <i>in proteo</i> models (at at ω B97X-D/SVP level) with constrained backbone atoms of Model G as derived from <i>TmeHydF</i> crystal structure with bridging apical cyanide coordination ($Z=-3$, $[4\text{Fe}-4\text{S}]^{2+} \times [\text{Fe}^{(\text{I})}\text{Fe}^{(\text{I})}]^{2-}$ open-shell singlet, spin polarized electronic state with total of 18 unpaired electrons, ‘abab’ spin coupling).	39
References for Supporting Information	40

1. Fourier-Transform Infrared Spectroscopic Results

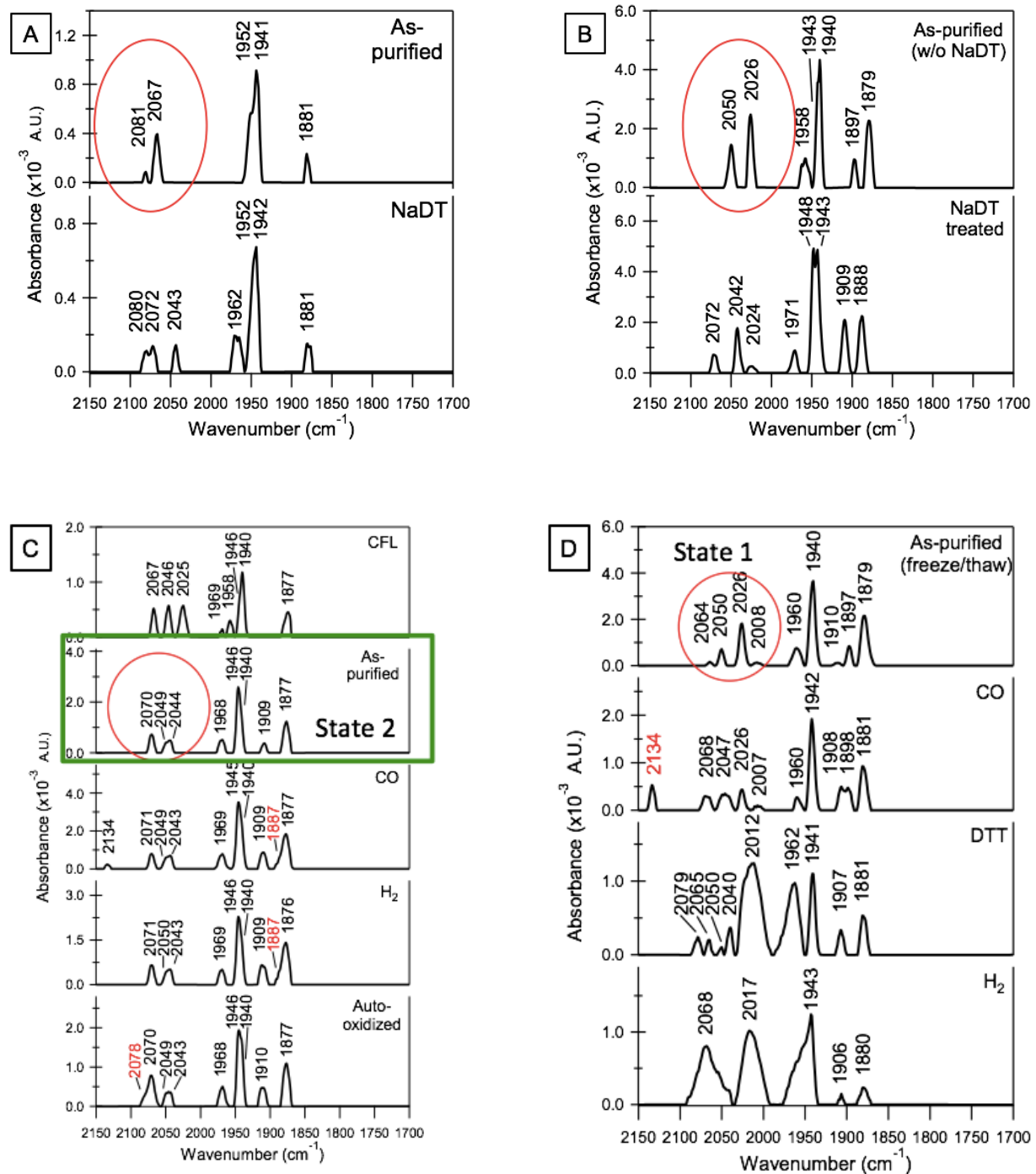


Figure S1.1: Low temperature (13 K) FTIR spectra of HydFEG. **A.** As-purified HydFEG (top panel, 1.8 mM protein with 2.10 ± 0.42 Fe/dimer) and in the presence of 10 mM DT (bottom panel, 1.6 mM protein with 2.10 ± 0.42 Fe/dimer). **B.** A distinct protein preparation of as-purified HydFEG (2.3 mM protein, undetermined Fe number) and DT treated protein (2.1 mM protein, undetermined Fe number, with 10 mM NaDT). **C.** Top panel shows the spectrum from the cell free lysate (CFL) of a distinct HydFEG expression. The remaining spectra refer to the purified HydFEG protein from this CFL in either as-purified, CO-treated, H₂-treated, or auto-oxidized states (2.1 mM protein, undetermined Fe number). **D.** Spectra refer to as-purified (without DT treatment) HydFEG, CO-treated, and H₂-treated enzyme (2.3 mM protein, undetermined Fe number). Also shown is the spectrum for as-purified HydFEG following addition of 10 mM dithiothreitol (DTT, 2.1 mM protein, undetermined Fe number).

2. Electron Paramagnetic Spectroscopic Results

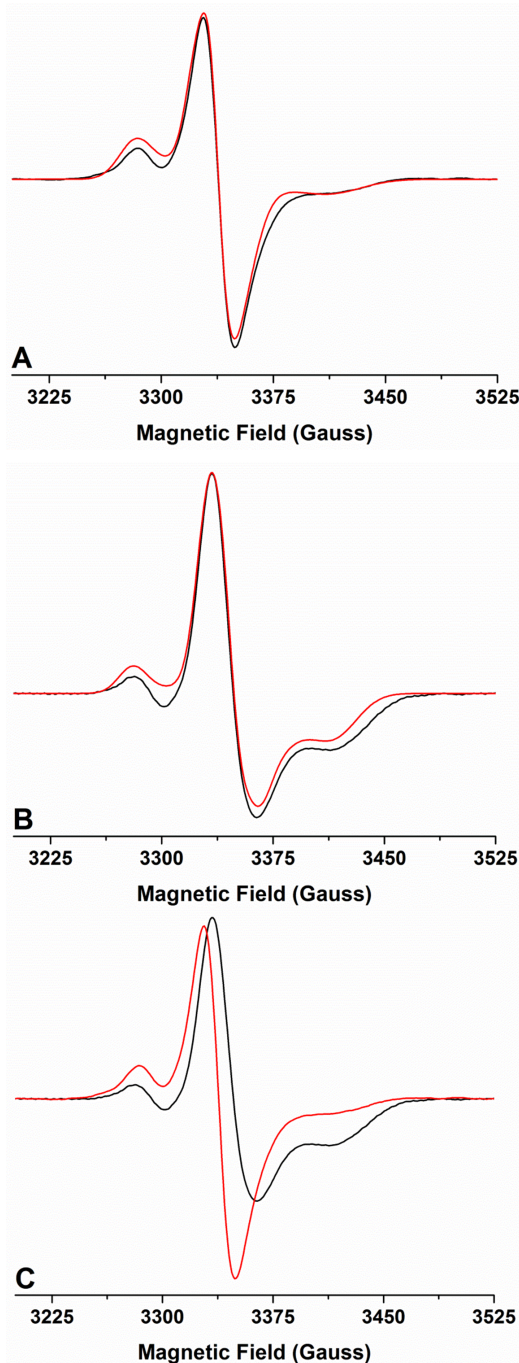


Figure S2.1: X-band EPR spectra of as-purified HydF^{EG} at 25 K. **A.** HydF^{EG} (335 μM protein with 3.22 ± 0.26 Fe/dimer) from a protein preparation that yielded FTIR observable bands. **B.** HydF^{EG} (310 μM protein with 4.36 ± 0.42 Fe/dimer) from a protein preparation that did not yield FTIR observable bands. In both panels **A** and **B**, the black spectrum corresponds to the experimental data, while the red line is the simulation. All simulations of experimental data were carried out using the EasySpin software platform¹¹ and generated the reported g-values presented in the text and supporting information (Table S2.1). In both panels **A** and **B**, the experimental signals are simulated as a mixture of two distinct [2Fe-2S]⁺ clusters; the details of these component signals are defined in Table S2.1. **C.** Direct overlay of the experimental spectra depicted in panels **A** (red spectrum) and **B** (black spectrum). We observe similar [4Fe-4S] clusters in HydF^{AEG} and HydF^{EG} (Fig. S2.2). However the [2Fe-2S] clusters we observe in HydF^{EG} are similar but not identical to those we observe in HydF^{AEG} (Table S2.1). At this time, while we do not currently understand the origin of these subtle differences, we presume that the structural flexibility of the conserved cysteine motif site influences the small g-value shifts associated with the [2Fe-2S]⁺ cluster signals; we have no reason to suspect that the EPR differences shown above are a result of [2Fe]_F loading.¹

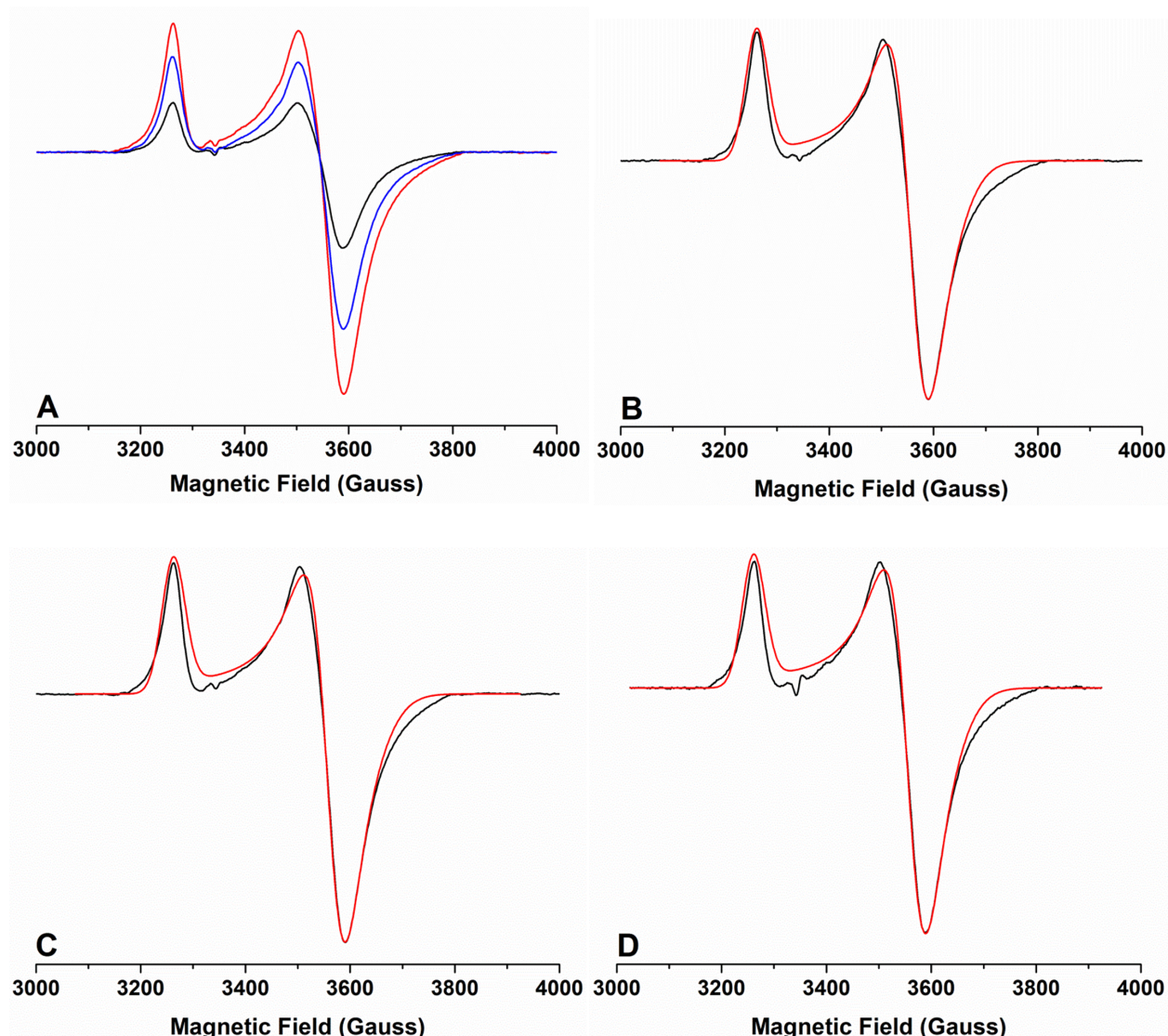


Figure S2.2: X-band EPR spectra of dithionite reduced HydF at 15 K. **A.** Direct overlay of experimental spectra for HydF^{EG} and HydF^{AEG}. Black spectrum represents 72 μ M HydF^{AEG} with 2.54 ± 0.04 Fe/dimer treated with 5 mM DT. Blue spectrum represents HydF^{EG} (335 μ M protein with 3.22 ± 0.26 Fe/dimer treated with 2 mM DT) from a protein preparation that yielded FTIR observable bands. Red spectrum represents HydF^{EG} (310 μ M protein with 4.36 ± 0.42 Fe/dimer treated with 2 mM DT) from a protein preparation that did not yield FTIR observable bands. Panels **B**, **C**, and **D**, show simulations (red lines) of the experimental data (black lines) depicted in panel **A**. All simulations of experimental data were carried out using the EasySpin software platform ¹¹ and generated the reported g-values presented in the text and supporting information (Table S2.1). Panel **B** is the simulation for the HydF^{EG} from a protein preparation that yielded FTIR observable bands. Panel **C** is the simulation for the HydF^{EG} from a protein preparation that did not yield FTIR observable bands. Panel **D** is the simulation for HydF^{AEG}.

Table S2.1. EPR spectroscopic properties of the [2Fe-2S]⁺ and [4Fe-4S]⁺ clusters associated with HydF^EG and HydF^AE^G. Values obtained via simulation with EasySpin as described in the main body. The [2Fe-2S]⁺ cluster g-values for HydF^AE^G were previously reported by us¹² and are included here again for convenience.

Enzyme	Cluster	Temperature	g ₁	g ₁ -strain	g ₂	g ₂ -strain	g ₃	g ₃ -strain
As-isolated HydF ^A E ^G	[2Fe-2S] ⁺ -#1	30 K	2.010	0.011	2.003	0.012	1.961	0.018
	[2Fe-2S] ⁺ -#2		2.045	0.015	2.008	0.017	1.981	0.024
DT Reduced HydF ^A E ^G	[4Fe-4S] ⁺	15 K	2.053	0.032	1.879	0.033	1.865	0.068
As-isolated HydF ^E G (I)	[2Fe-2S] ⁺ -#1	25 K	2.016	0.010	2.004	0.008	1.961	0.028
	[2Fe-2S] ⁺ -#2		2.041	0.016	2.008	0.008	1.997	0.015
DT Reduced HydF ^E G (I)	[4Fe-4S] ⁺	15 K	2.054	0.032	1.879	0.032	1.864	0.071
As-isolated HydF ^E G (II)	[2Fe-2S] ⁺ -#1	25 K	2.011	0.012	2.001	0.011	1.960	0.021
	[2Fe-2S] ⁺ -#2		2.042	0.014	1.992	0.010	1.981	0.028
DT Reduced HydF ^E G (II)	[4Fe-4S] ⁺	15 K	2.052	0.033	1.878	0.032	1.863	0.071

(**I**). Spectral analysis of protein from a preparation that yielded FTIR observable bands. (**II**). Spectral analysis of protein from a preparation that did not yield FTIR observable bands.

3. Computational Modeling and Structure Refinement

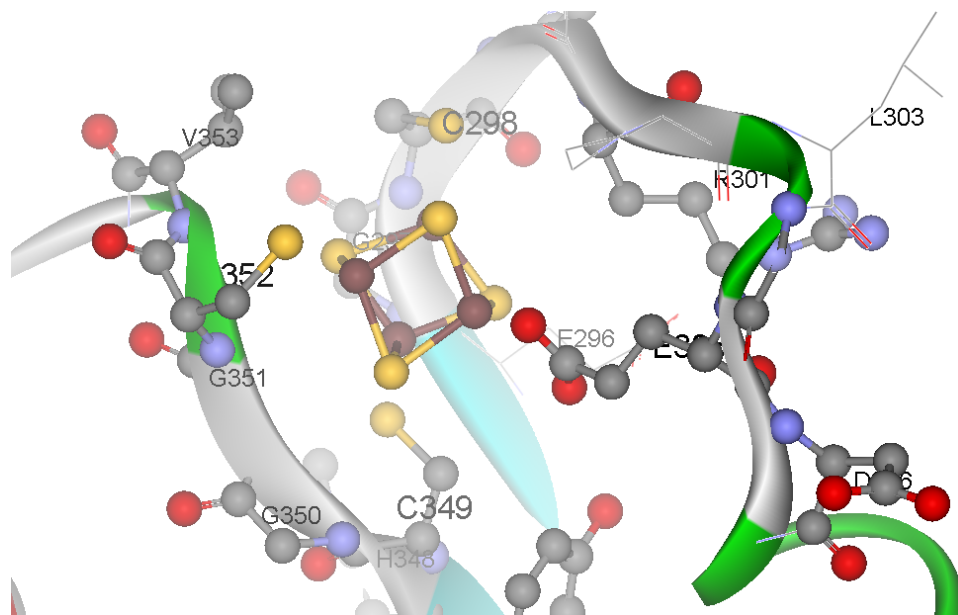


Figure S3.1: The experimental structure of [4Fe-4S] cluster and its inner sphere protein environment taken from the 2.8 Å resolution structure (5KH0) of HydF from *Thermosiphon melanesiensis* (Ref. 1).

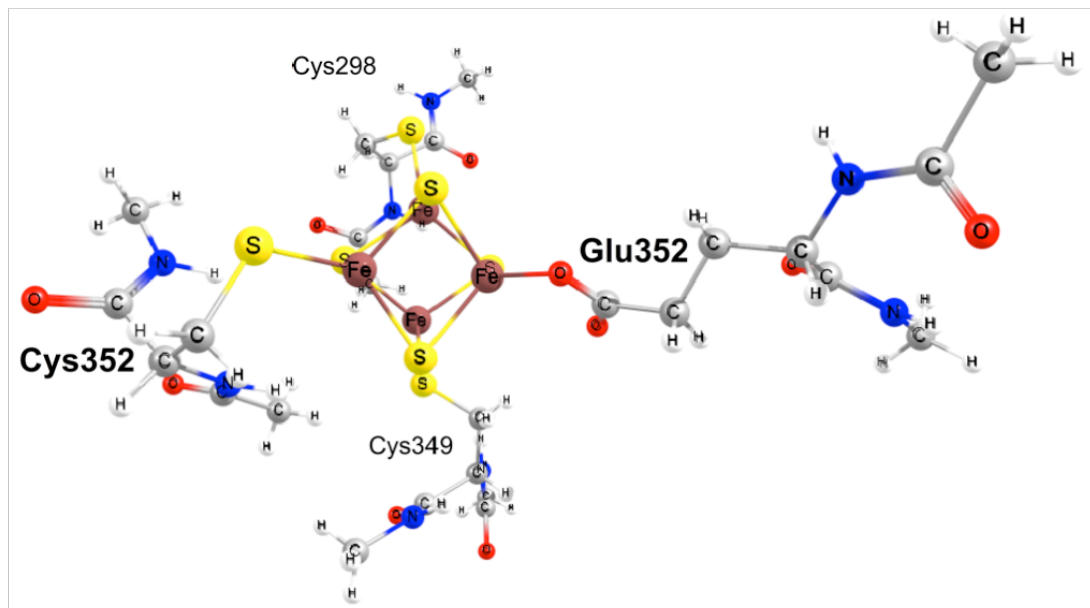


Figure S3.2: The excised [4Fe-4S] cluster with inner-sphere ligands including peptide bonds from adjacent amino acids justified by the presence of H-bonding and peptide dipoles with the [4Fe-4S] cluster.

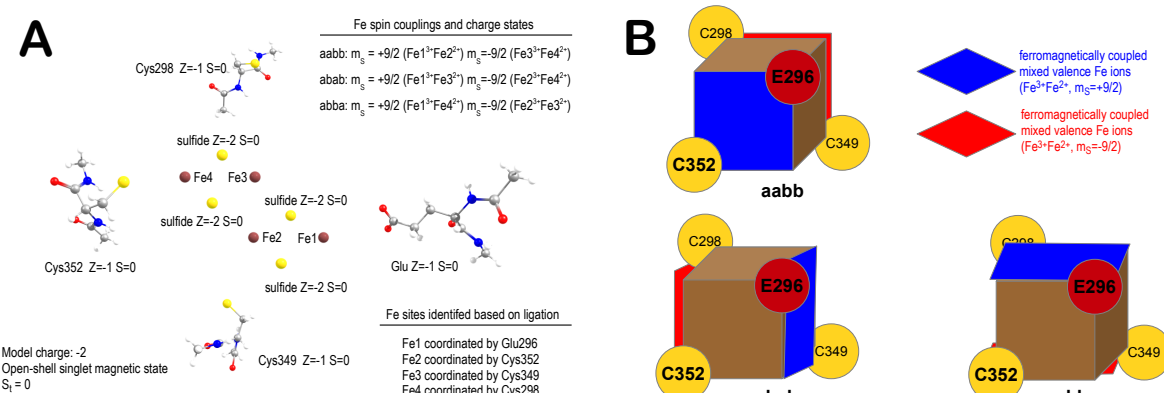


Figure S3.3: Ionic fragment decomposition (A) and spin coupling schemes (B) considered.

Table S3.1: Energy changes (ΔE^{SCF} in kJ mol⁻¹) as a function of refinement steps of the [4Fe-4S] cluster model from Figure S3.2 calculated at ω B97X-D/SVP level.

optimized moiety	$\Delta E^{\text{SCF}}(\text{aabb})$	$\Delta E^{\text{SCF}}(\text{abab})$	$\Delta E^{\text{SCF}}(\text{abba})$
none, X-ray structure	+1077	+1073	+1070
[Fe ₄ S ₄ S ₃], <i>in vacuo</i>	+1030	+1029	+1023
inner sphere, ^a <i>in vacuo</i>	+798	+796	+793
unconstrained, <i>in vacuo</i>	+26	0 ^b	+27
inner sphere, ^a <i>in proteo</i>	+186	+183	+185
unconstrained, <i>in proteo</i>	-401	-394	-406

^a [Fe₄S₄(SCH₂)₃(OOCH₂CH₂)]; ^b -10048.0742874 a.u.

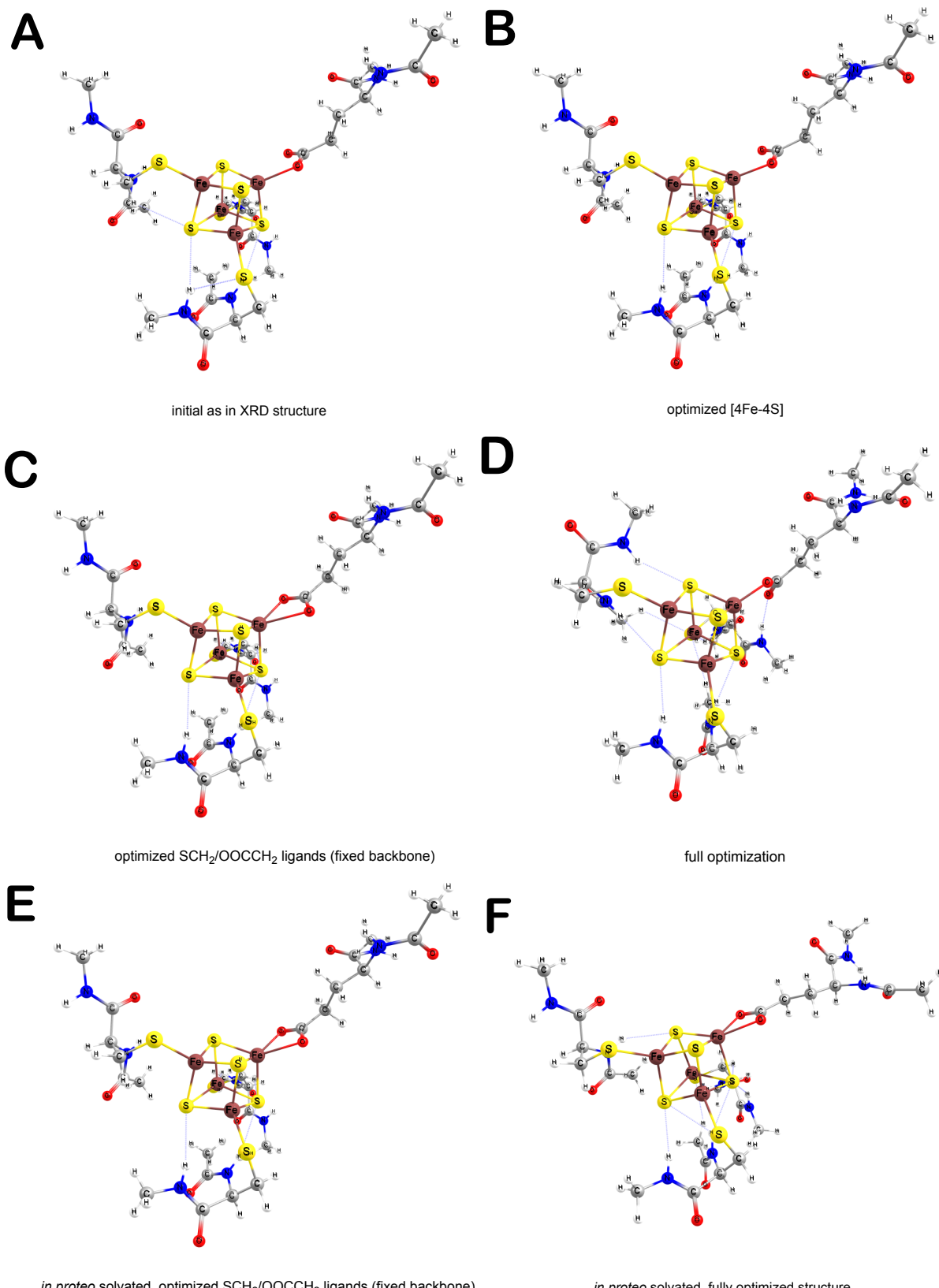


Figure S3.4: Structural changes as a function of refinement steps for the [4Fe-4S] cluster model from Figure S3.2 calculated at ω B97X-D/SVP level and illustrated here for the ‘abab’ coupling (Figure S3.3B).

4. Calculated Vibrational Spectra for [2Fe] Synths

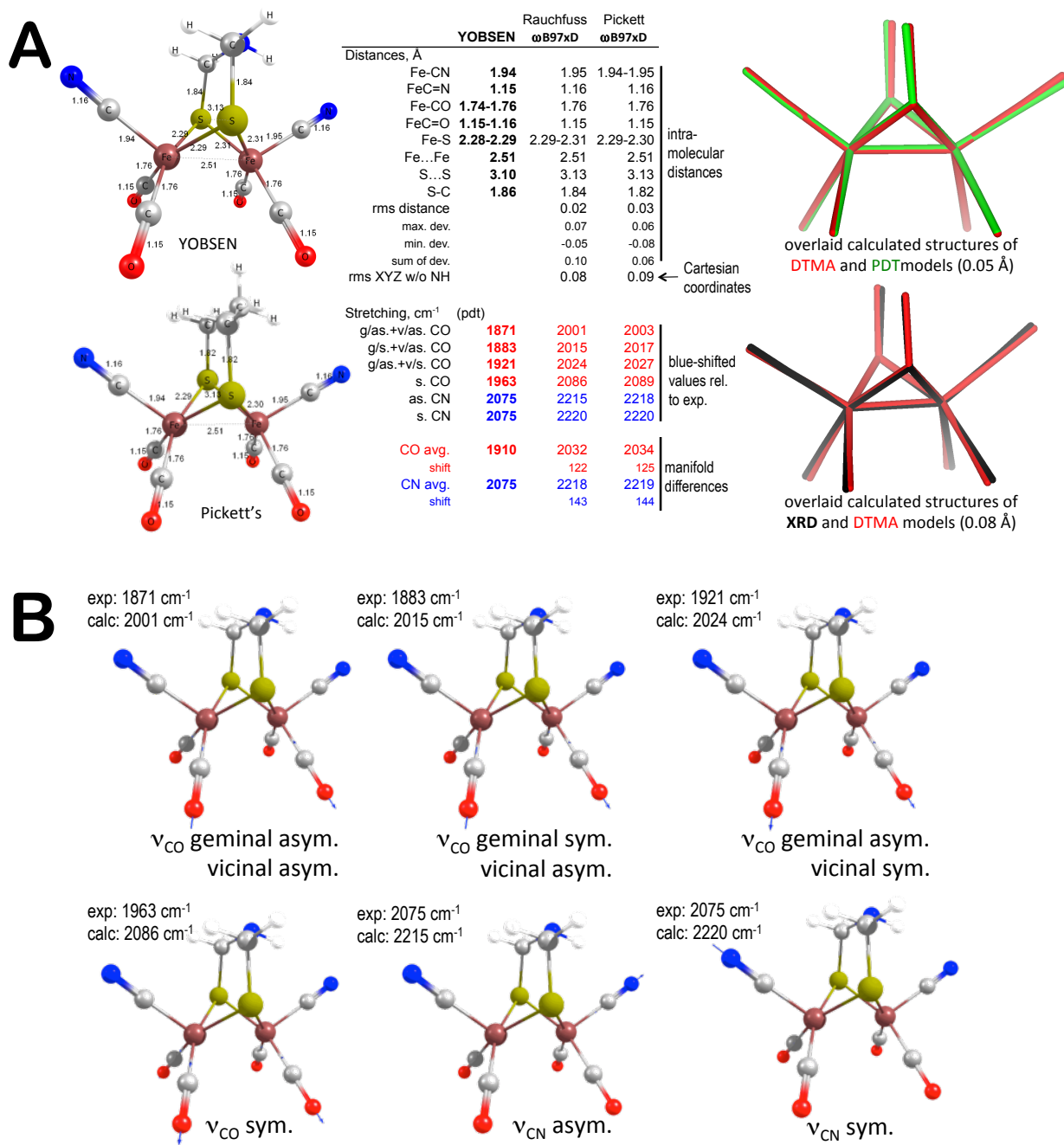


Figure S4.1: Comparison of the performance of ωB97X-D functional using def2TZVP all-electron basis set (A) for Rauchfuss (YOBSEN with DTMA ligand, Ref. ²) and Pickett (no XRD structure with PDT ligand, Ref. ³) without employing scaled quantum chemical force field correction and (B) assignment of diatomic stretching vibrational modes calculated at the same level.

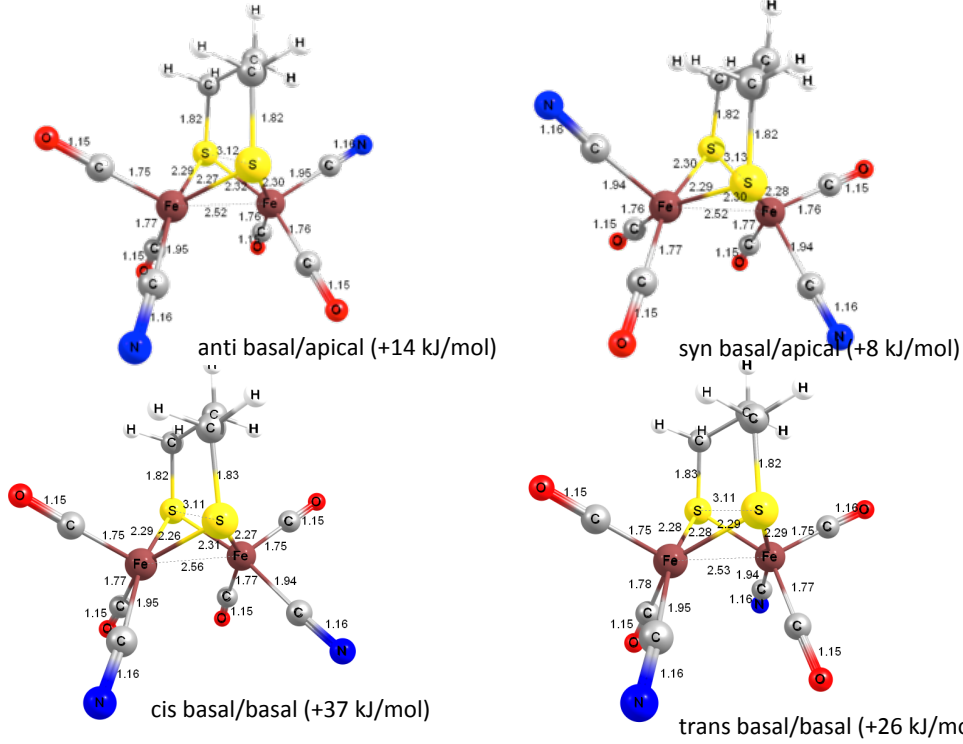


Figure S4.2: Graphical illustration of structural and energetic differences for coordination isomers of $[\text{Fe}_2(\text{DTMA})(\text{CO})_4(\text{CN})_2]^{2-}$ complex at $\omega\text{B97X-D/def2TZVP}$ level using X-ray structure YOBSEN (apical/apical isomer), Ref² and WOLROE (apical/basal isomer), Ref⁴.

Table S4.1: Comparison of geometric structure, relative energies, and diatomic stretching frequencies without a force field correction for coordination isomers of $[\text{Fe}_2(\text{DTMA})(\text{CO})_4(\text{CN})_2]^{2-}$ complex at $\omega\text{B97X-D/def2TZVP}$ level using X-ray structure YOBSEN (apical/apical isomer), Ref² and WOLROE (apical/basal isomer), Ref⁴.

	YOBSEN	WOLROE	anti api/api	syn bas/api to YOBSEN	cis bas/bas to WOLROE	trans bas/bas to YOBSEN
Distances, Å						
Fe-CN	1.94	1.94	1.94-1.95	1.95	1.94	1.94-1.95
FeC=N	1.15	1.14	1.16	1.16	1.16	1.16
Fe-CO	1.74-1.76	1.71/1.77	1.76	1.75-1.77	1.76-1.77	1.75-1.77
FeC=O	1.15-1.16	1.16/1.19	1.15	1.15	1.15	1.15-1.16
Fe-S	2.28-2.29	2.27	2.29-2.30	2.27-2.32	2.28-2.30	2.26-2.31
Fe...Fe	2.51	2.52	2.51	2.52	2.52	2.56
S...S	3.10	3.09	3.13	3.12	0.23	3.11
S-C	1.86	1.82-1.83	1.82	1.82	1.82	1.82-1.83
rms distance	0.03	0.03	0.03	0.03	0.03	0.02
max. dev.	0.06	0.06	0.06	0.06	0.10	0.06
min. dev.	-0.07	-0.08	-0.08	-0.08	-0.09	-0.07
sum of dev.	-0.07	0.06	0.05	0.05	0.13	0.05
rms XYZ w/o NH	0.23	0.09	0.18	0.26	0.15	0.31
SCF energies, a.u.						
relative energies, kJ/mol	-4081.11	-4081.10		-4081.10	-4081.09	-4081.10
	0	14		8	37	26
Stretching, cm ⁻¹						
Pickett	1871	1867	2003	1992	1990	1986
in KBr						1992
g/as.+v/as. CO	1883	1880	2017	2014	2009	1998
g/s.+v/as. CO	1921	1917	2027	2040	2036	2015
g/as.+v/s. CO	1963	1951	2089	2089	2087	2082
s. CO	2075	2029	2218	2218	2216	2090
as. CN						2087
s. CN	2078	2220	2225	2227	2235	2229
CO avg. shift	1910	1904	2034	2034	2031	2020
			125	124	121	111
CN avg. shift	2075	2054	2219	2222	2222	2234
			144	147	147	168
					159	153
						150
					average	st. dev
						range
					6	17
					9	19
					12	29
					3	8
					7	16
					5	15

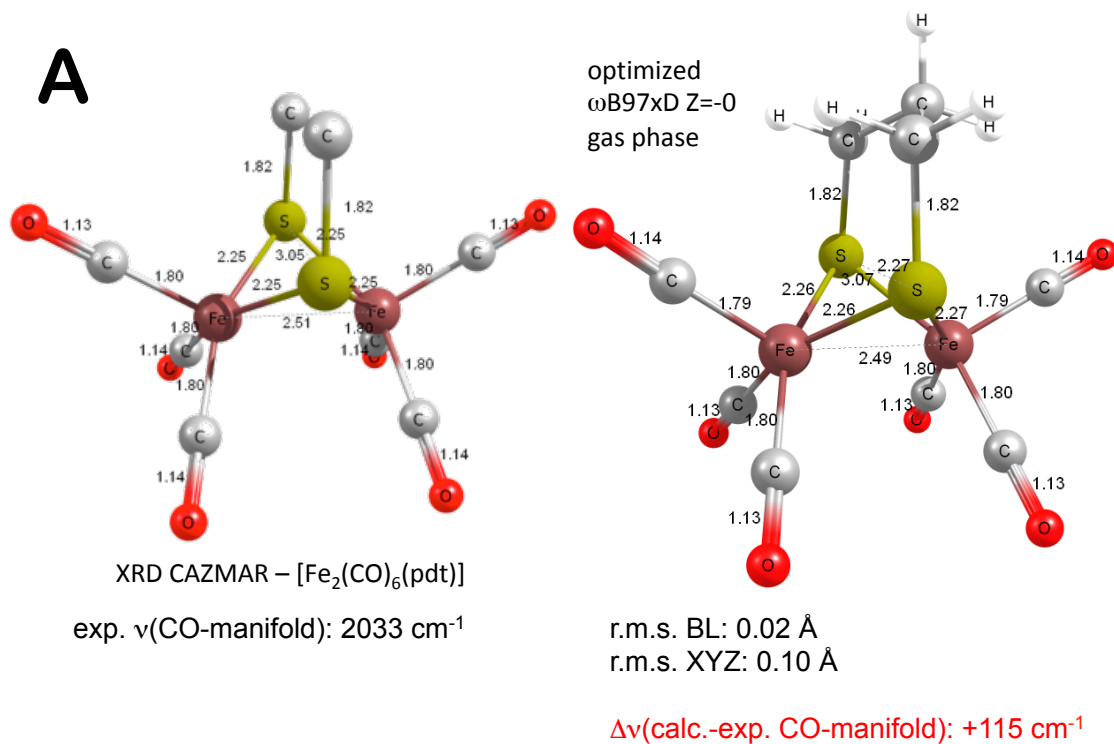
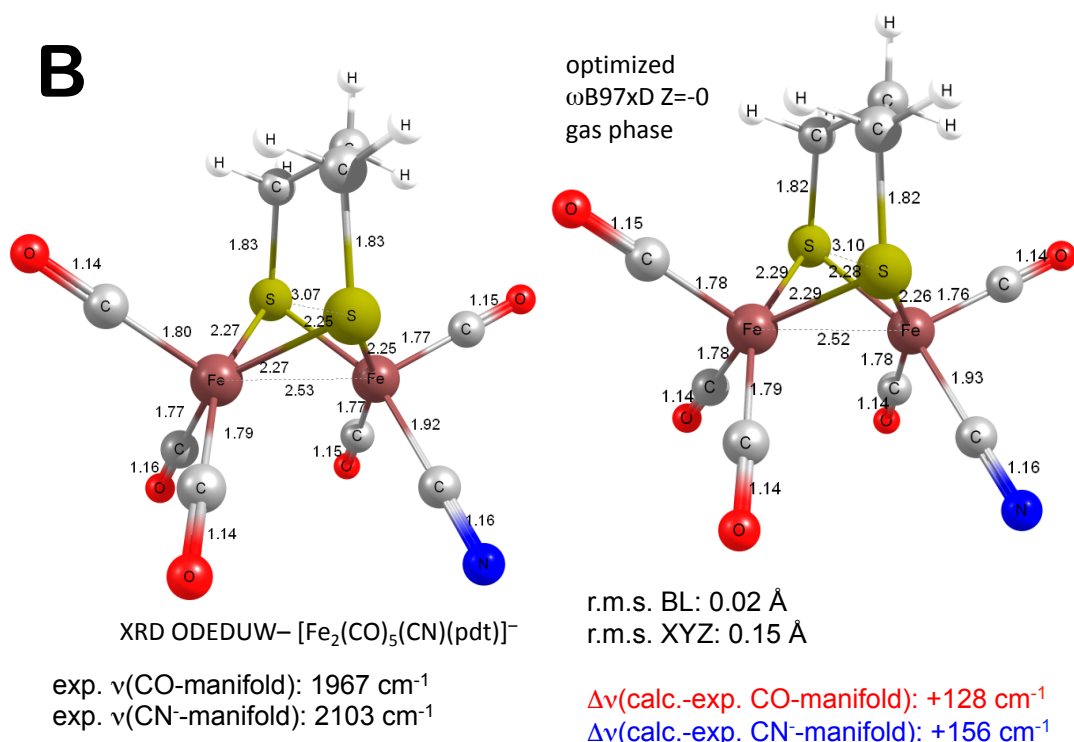
A**B**

Figure S4.3: Comparison of optimized structure and diatomic stretching frequencies without a force field correction for crystallographically characterized isomers of $[\text{Fe}_2(\text{dithiolate})(\text{CO})_{5-6}(\text{CN})_{1-0}]^{1/0}$ complexes at ω B97X-D/def2TZVP level using X-ray structure CAZMAR (Ref. 5), and ODEDUW (Ref. 6).

Table S4.2: Compilation of optimized structures and diatomic stretching frequencies calculated at generalized graduate approximation (GGA, pure and hybrid),

metaGGA, double-hybrid (DH) density functional and wave function (Ψ) level using def2TZVP basis set.

	GGA				metaGGA			DH		Ψ	
	YOBSEN	BP86	B(5HF)P86	B3LYP	B(50HF)LYP	TPSS	ω B97xD	M06x	B2PLYPD3	MP2	HF
Distances, Å											
Fe-CN	1.94	1.92-1.93		1.92	1.95	1.90	1.93	1.95	2.01	1.90-1.91	1.75-1.76
FeC=N	1.15	1.18		1.18	1.17	1.15	1.18	1.16	1.16	1.18	1.20
Fe-CO	1.74-1.76	1.75	1.74-1.75		1.76	1.75	1.75	1.76	1.83-1.84	1.69-1.70	1.57-1.58
Fe=C=O	1.15-1.16	1.17-1.18		1.17	1.16	1.13	1.17	1.15	1.14	1.18	1.20
Fe-S	2.28-2.29	2.30-2.31	2.29-2.30	2.33-2.34		2.27-2.28	2.29-2.30	2.29-2.31	2.40-2.41	2.26	2.14-2.15
Fe...Fe	2.51	2.60		2.57	2.57	2.45	2.57	2.51	2.52	2.55	2.46
S...S	3.10	3.11		3.11	3.16	3.11	3.11	3.13	3.30	3.06	2.90
S-C	1.86	1.88		1.86	1.86	1.81	1.87	1.84	1.84	1.86	1.85
rms distance		0.03		0.03	0.05	0.04	0.03	0.02	0.15	0.06	0.22
max. abs. dev.		0.10		0.08	0.20	0.02	0.06	0.07	0.49	0.08	0.18
min. abs. dev.		-0.03		-0.04	0.00	-0.10	-0.02	-0.05	-0.06	-0.20	-0.69
sum of dev.		0.31		0.22	0.41	-0.32	0.25	0.10	1.10	-0.22	-1.62
rms XYZ w/o NH		0.20		0.18	0.12	0.09	0.16	0.08	0.14	0.27	0.44
(DTMA) Stretching, 1/cm											
1916	(PDT)										
1921	1871	1863		1892	1945	2098	1873	2001	2011	1890	1780
1953	1883	1879		1908	1965	2106	1891	2015	2035	1907	1800
1984	1921	1899		1927	1965	2131	1908	2024	2064	1980	1912
1987	1963	1940		1968	2026	2188	1952	2086	2124	1994	1991
2037	2075	2064		2086	2171	2310	2086	2215	2243	2112	2018
2042	2075	2071		2093	2177	2314	2092	2220	2244	2115	2271
CO avg.	1910	1895		1924	1975	2131	1906	2032	2059	1943	1871
shift		-14		14	66	221	-4	122	149	33	-39
CN avg.	2075	2068		2090	2174	2312	2089	2218	2244	2114	2145
shift		-8		15	99	237	14	143	169	39	70
											340

5. Development of Scaled Quantum Chemical Force Fields

Scaling/shifting factors from literature

BP86/TZVP:	$v(\text{adj.}) = v(\text{calc.}) - 2 \text{ cm}^{-1}$	$R^2 = 0.970$	Ref. 7
	$v(\text{adj.}) = 0.999 v(\text{calc.})$	$R^2 = 0.970$	
	$v(\text{adj.}) = 0.955 v(\text{calc.}) + 88 \text{ cm}^{-1}$	$R^2 = 0.972$	

B3LYP/DZP:	$v(\text{adj.}) = 0.9538 v(\text{calc.})$	$R^2 = 0.9477$	Ref. 8-9
------------	---	----------------	----------

Scaling/shifting factors of the given study

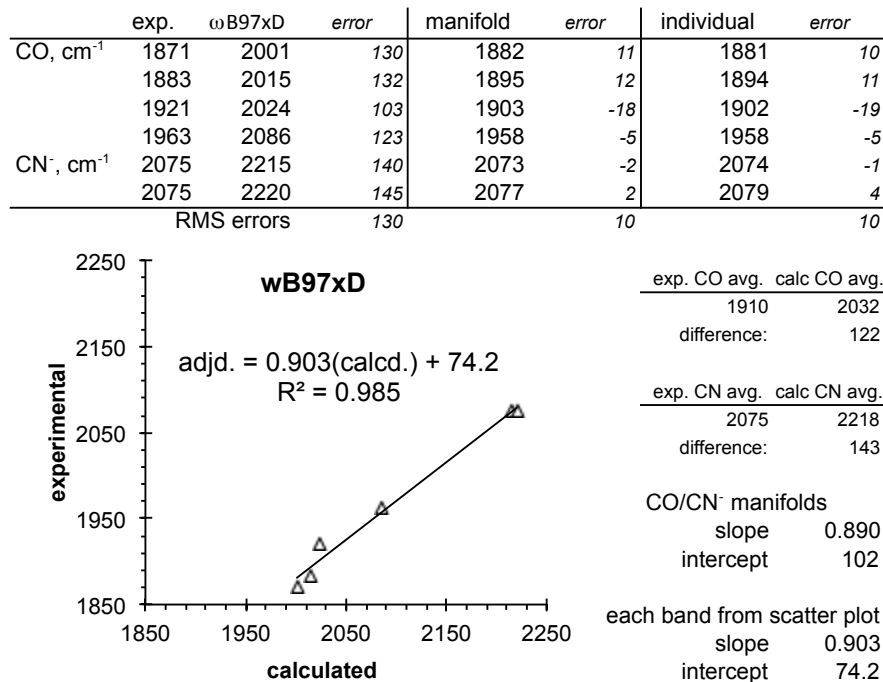
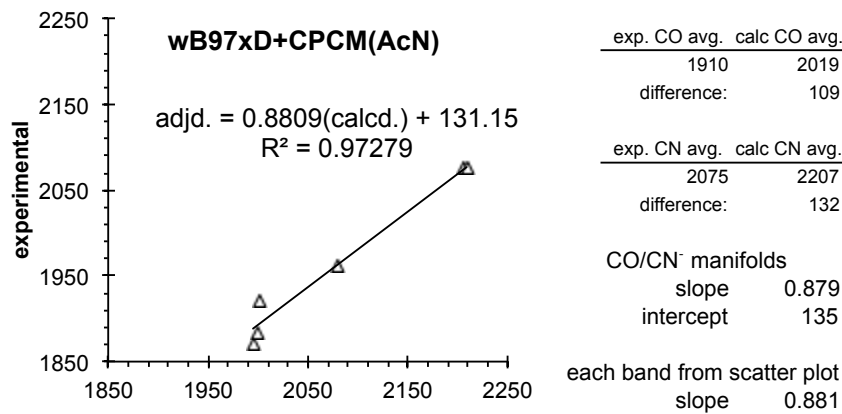


Figure S5.1: Summary of scaled quantum chemical force fields from literature (Refs. 7-9) and our work.

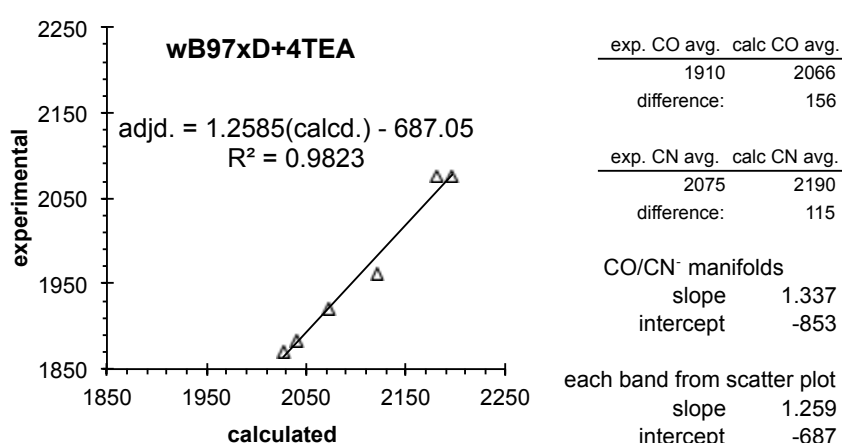
A

	exp.	ω B97xD	error	manifold	error	individual	error
CO, cm^{-1}	1871	1995	124	1889	18	1889	18
	1883	1999	116	1892	9	1892	9
	1921	2001	80	1894	-27	1894	-27
	1963	2080	117	1963	0	1963	0
	CN ⁻ , cm^{-1}		2075	2205	130	2073	-2
	2075		2209	2077	2	2077	2
RMS errors			118		14		14



B

	exp.	ω B97xD	error	manifold	error	individual	error
CO, cm^{-1}	1871	2027	156	1858	-13	1864	-7
	1883	2041	158	1876	-7	1882	-1
	1921	2073	152	1919	-2	1922	1
	1963	2122	159	1985	22	1983	20
	CN ⁻ , cm^{-1}		2075	2182	107	2065	-10
	2075		2197	2085	10	2059	-16
RMS errors			144		12		11



C

	exp.	SVP	error	manifold	error	individual	error
CO, cm^{-1}	1871	2027	156	1884	13	1882	11
	1883	2037	154	1893	10	1891	8
	1921	2051	130	1905	-16	1904	-17
	1963	2111	148	1957	-6	1957	-6
	CN ⁻ , cm^{-1}		2075	2245	170	2074	-1
	2075		2248	2076	1	2078	3
RMS errors			156		10		10

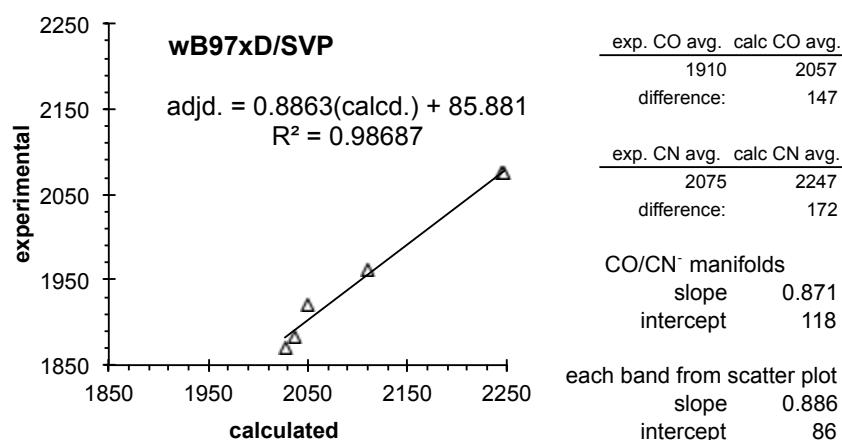
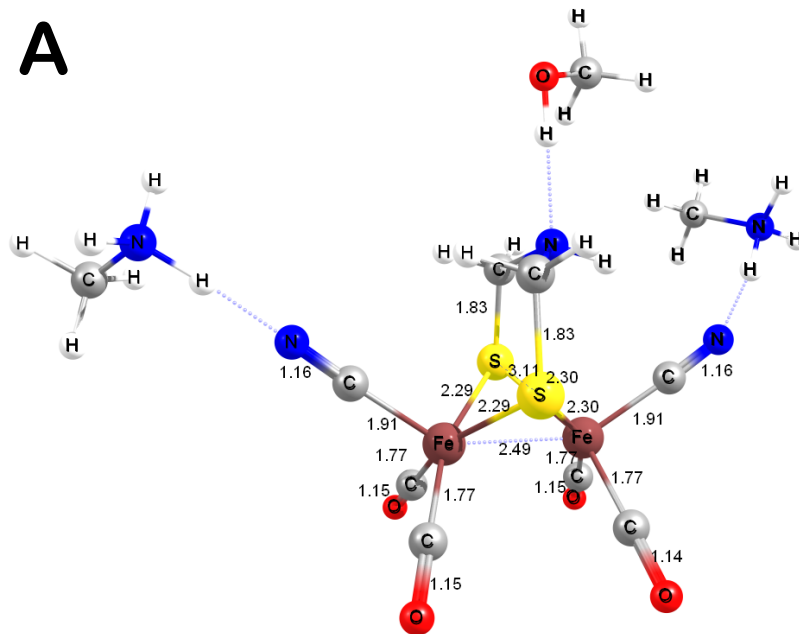


Figure S5.2: Dependence of scaling and shifting factors developed for scaled quantum chemical force fields as a function of presence of implicit (A), both explicit counter ion and implicit solvent environment (B) and using a smaller yet reliable basis set (C) for electronic structure calculation of the [4Fe-4S] cluster models.

6. Geometric, Energetic, and Vibrational Analyses of Model A



B

(as purified) State 2		Non specific binding at protein surface		
Distances, Å		RMS Cartesian 0.068 Å to YOBSEN		
Fe-CN	1.91			
FeC=N	1.16			
Fe-CO	1.77			
Fe-C=O	1.14-1.15			
Fe-S	2.29-2.30			
Fe...Fe	2.49			
S...S	3.11			
S-C	1.83			
E, a.u.	-4405.83			
ΔE, kJ mol ⁻¹				
Stretching, cm ⁻¹		corrected TEA+PCM	corrected gas phase	corrected PCM only
1877	2020	1907	1899	1911
1909	2025	1911	1904	1915
(1940)	2026	1912	1905	1916
1946	2026	1912	1905	1916
1968	2095	1976	1966	1977
(2049)	2044	2073	2060	2070
2044	2201	2073	2060	2070
2070	2215	2086	2073	2082
CO avg. shift	1925 40	2042 132	1927 2 -7 -8 -9	1918 5 -7 -8 -9
CN avg. shift	2057	2208 133	2080 23	2067 10 19

Figure S6.1: Optimized structure (A, at ω B97X-D/def2TZVP level) for $[\text{Fe}^{(\text{I})}\text{Fe}^{(\text{I})}]^{2-}$ Model A, non-specific binding at an arbitrary protein binding pocket and (B) calculated intramolecular distances and scaled diatomic stretching frequencies in comparison to the experimental HydF^{EG} bands.

7. Geometric, Energetic, and Vibrational Analyses of Models B

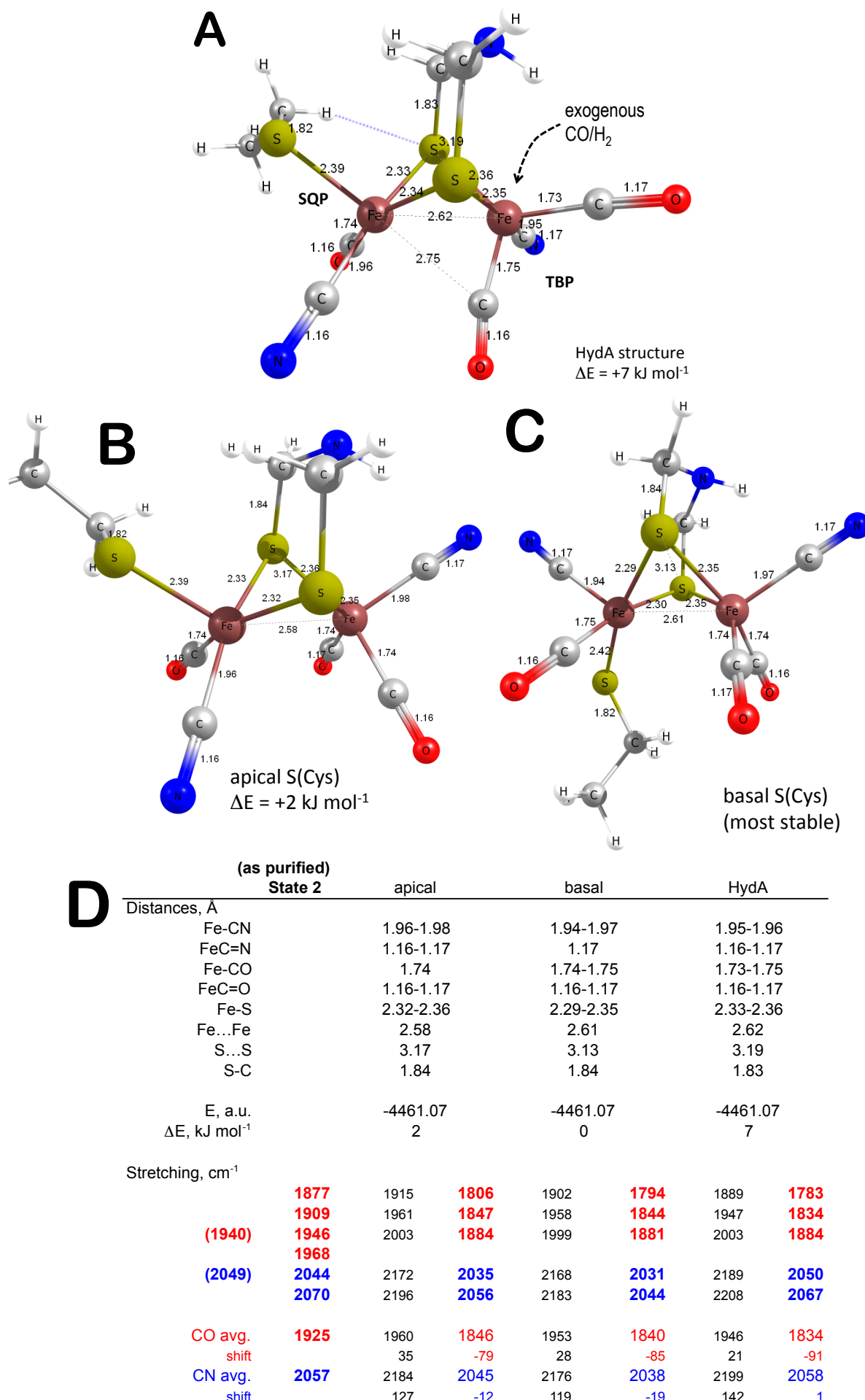
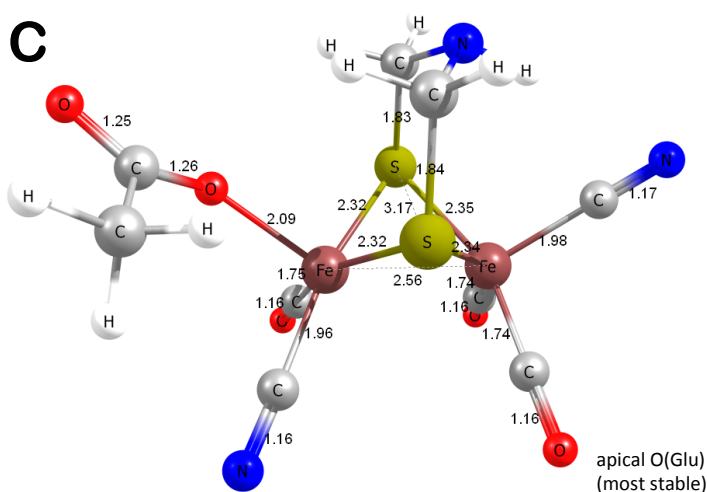
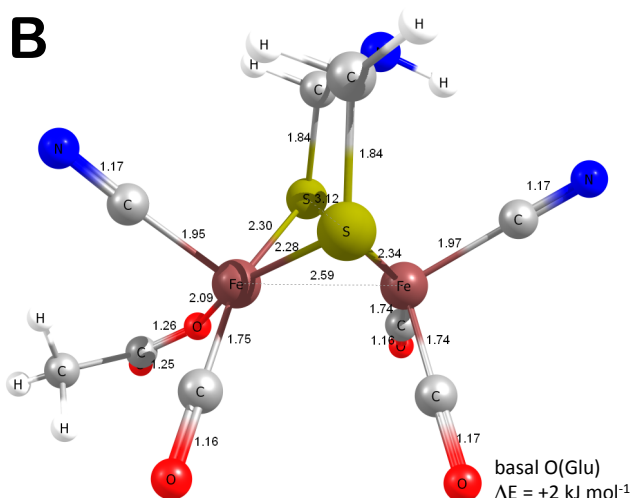
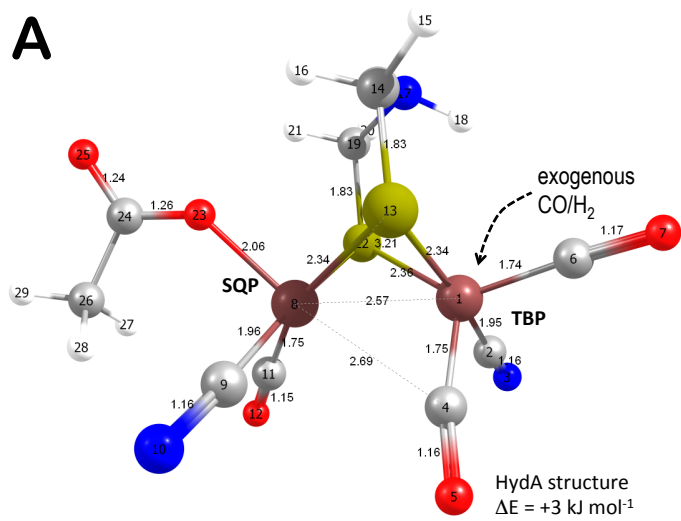


Figure S7.1: Optimized structures (A-C, at ωB97X-D/def2TZVP level) for $[\text{Fe}^{(\text{I})}\text{Fe}^{(\text{I})}]^{2-}$ **Model B-Cys**, loss of CO from **Model A** and $[2\text{Fe}]_{\text{F}}$ cluster model binding via a protein derived cysteine ligand and (D) calculated intramolecular distances and scaled diatomic stretching frequencies in comparison to the experimental HydF^{EG} bands.



D (as purified)

	State 2	apical	basal	HydA				
Distances, Å								
Fe-CN		1.96-1.98	1.95-1.97	1.95-1.96				
Fe-C≡N		1.16-1.17	1.17	1.16				
Fe-CO		1.74-1.75	1.74-1.75	1.74-1.75				
Fe-C=O		1.16	1.16-1.17	1.15-1.17				
Fe-S		2.32-2.235	2.28-2.34	2.34-2.36				
Fe...Fe		2.56	2.59	2.57				
S...S		3.17	3.12	3.21				
S-C		1.83-1.84	1.84	1.83				
E, a.u.		4212.16	4212.16	4212.16				
$\Delta E, \text{kJ mol}^{-1}$		0	2	3				
Stretching, cm ⁻¹								
		1877 1909 (1940) 1968 (2049) 2044 2070	1929 1970 2022 2039 2177 2196	1818 1855 1901 2039 2173 2185	1918 1973 2016 2035 2179 2179	1809 1857 1896 2035 2046 2041	1898 1946 2022 2193 2207 2200	1791 1833 1901 2053 2066 2059
CO avg. shift		1925 2057	1974 49 2187	1858 -67 2047	1969 44 2179	1854 -71 2041	1955 30 2200	1842 -83 2059
CN avg. shift			130	-10	122	-16	143	2

Figure S7.2: Optimized structures (A-C, at ωB97X-D/defTZVP level) for $[\text{Fe}^{(\text{I})}\text{Fe}^{(\text{I})}]^2-$ **Model B-Glu/Asp**, loss of CO from **Model A** and $[2\text{Fe}]_F$ cluster model binding via a protein derived glutamate/aspartate ligand and (D) calculated intramolecular distances and scaled diatomic stretching frequencies in comparison to the experimental HydF^{EG} bands.

8. Geometric, Energetic, and Vibrational Analyses of Models C

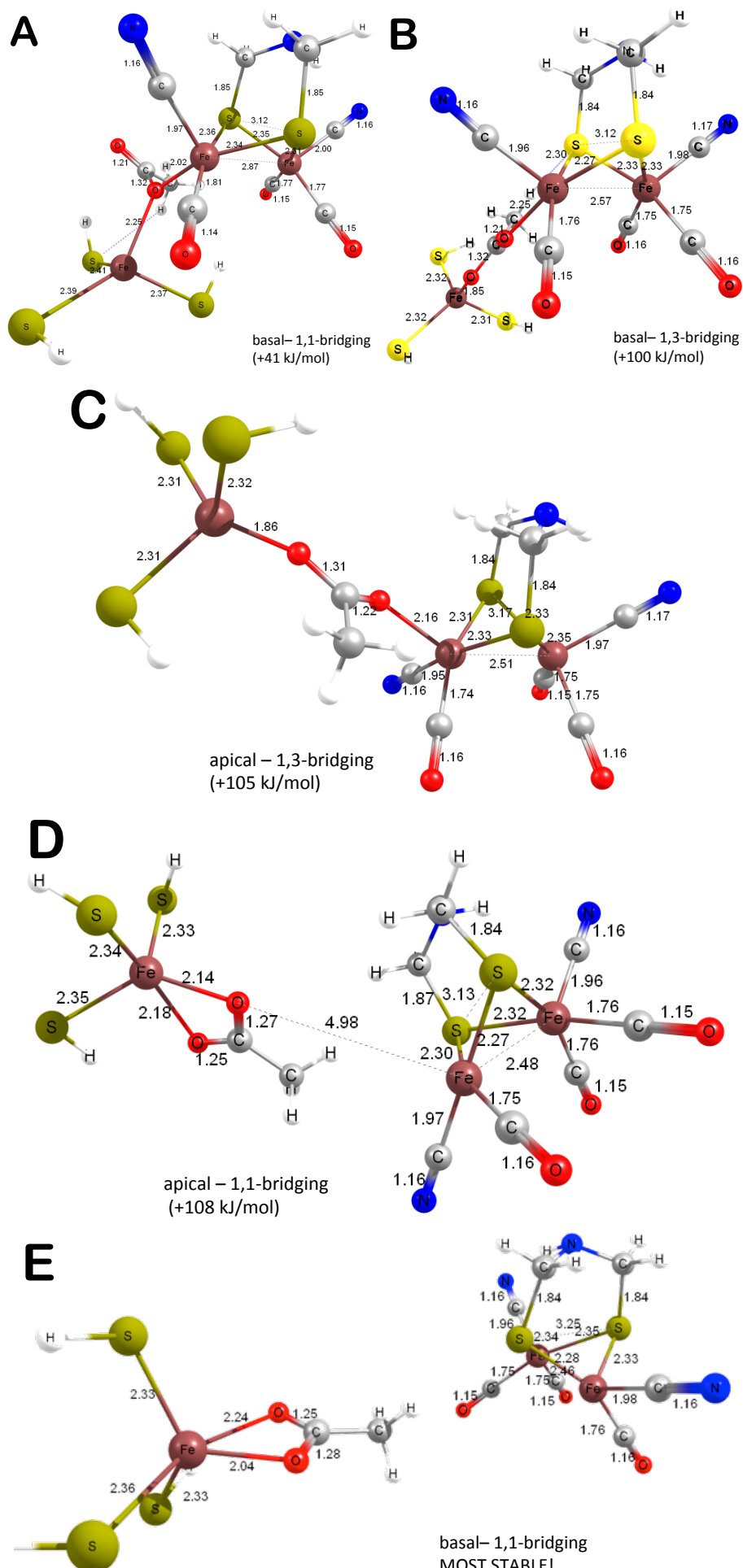


Figure S8.1: Optimized structures (A-E, at ω B97X-D/def2TZVP level) for $[Fe^{(II)}Fe^{(II)}]^{2+}$ **Model C-Glu/Asp**, loss of CO from **Model A**, $[2Fe]_F$ cluster model binding via a bridging glutamate/aspartate ligand to a ‘unique Fe site’ (modeled by $[Fe^{3+}(SH)_3]$) and (F) calculated intramolecular distances and scaled diatomic stretching frequencies in comparison to the experimental HydF^{EG} bands

F	(as purified) State 2	basal 1,1 bridging	basal 1,3 bridging	apical 1,1 bridging	apical 1,1 bridging	apical 1,3 bridging			
Distances, Å									
Fe-CN		1.97, 1.96	1.96-1.98	2.01, 1.96	1.97, 2.00	1.95, 1.97			
FeC=N		1.16	1.16-1.17	1.16	1.16	1.16, 1.17			
Fe-CO		1.75, 1.76	1.76-1.75	1.75-1.76	1.81, 1.77	1.74, 1.75			
FeC=O		1.16, 1.15	1.15-1.16	1.15-1.16	1.14, 1.15	1.16			
Fe-S		2.27-2.30, 2.32	2.27-2.33	2.31-2.34, 2.33-2.35	2.34-2.36, 2.31-2.35	2.31/2.33, 2.33/2.35			
Fe...Fe		2.48	2.57	2.52	2.87	2.51			
S...S		3.13	3.12	3.24	3.12	3.17			
S-C		1.84, 1.87	1.84	1.84	1.85	1.84			
E, a.u.		-6672.51	-6672.51	-6672.55	-6672.53	-6672.51			
ΔE, kJ mol⁻¹		108	100	0	41	105			
Stretching, cm⁻¹									
	1877	dissociated	1951	1838	dissociated	2025	1904	1948	1835
	1909		1962	1848		2077	1950	1986	1869
(1940)	1946		2037	1914		2135	2002	2038	1915
	1968								
(2049)	2044		2188	2049		2207	2066	2191	2051
	2070		2200	2059		2229	2085	2213	2071
CO avg. shift	1925		1983	1867		2135	1952	2075	1873
			58	-58		210	27	150	-52
CN avg. shift	2057		2194	2054		2218	2075	2202	2061
			137	-3		161	18	145	4

Figure S8.1 continued.

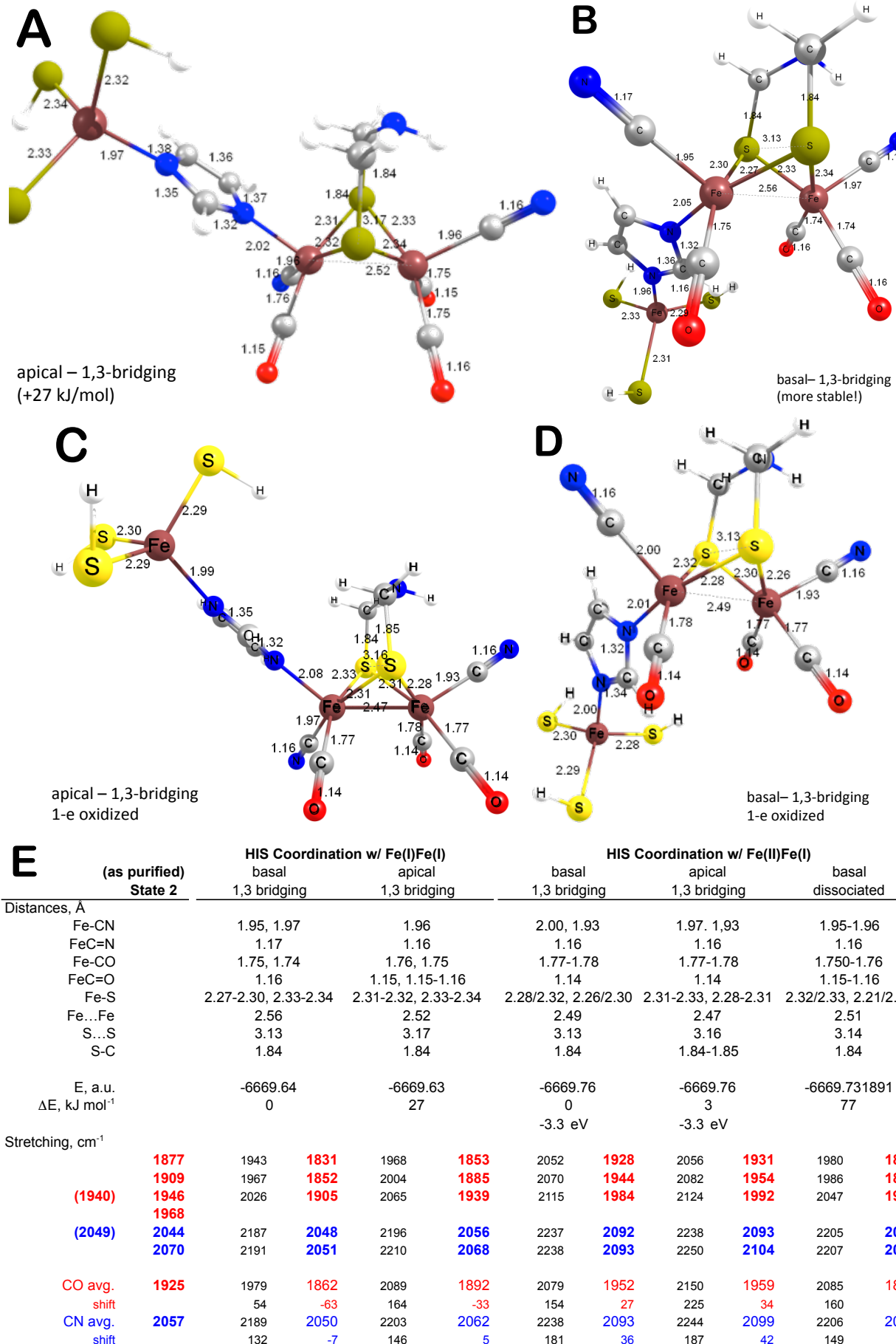


Figure S8.2: Optimized structures (at ω B97X-D/def2TZVP level) for reduced $[Fe^{(I)}Fe^{(I)}]^{2-}$ (A-B) and oxidized $[Fe^{(I)}Fe^{(II)}]^-$ (C-D) Model C-His, loss of CO from Model A, $[2Fe]_F$ cluster model binding via a bridging histidine ligand to a ‘unique Fe site’ (modeled by $[Fe^{3+}(SH)_3]$) and (E) calculated intramolecular distances and scaled diatomic stretching frequencies in comparison to the experimental HydF^{EG} bands.

9. Geometric, Energetic, and Vibrational Analyses of Models D

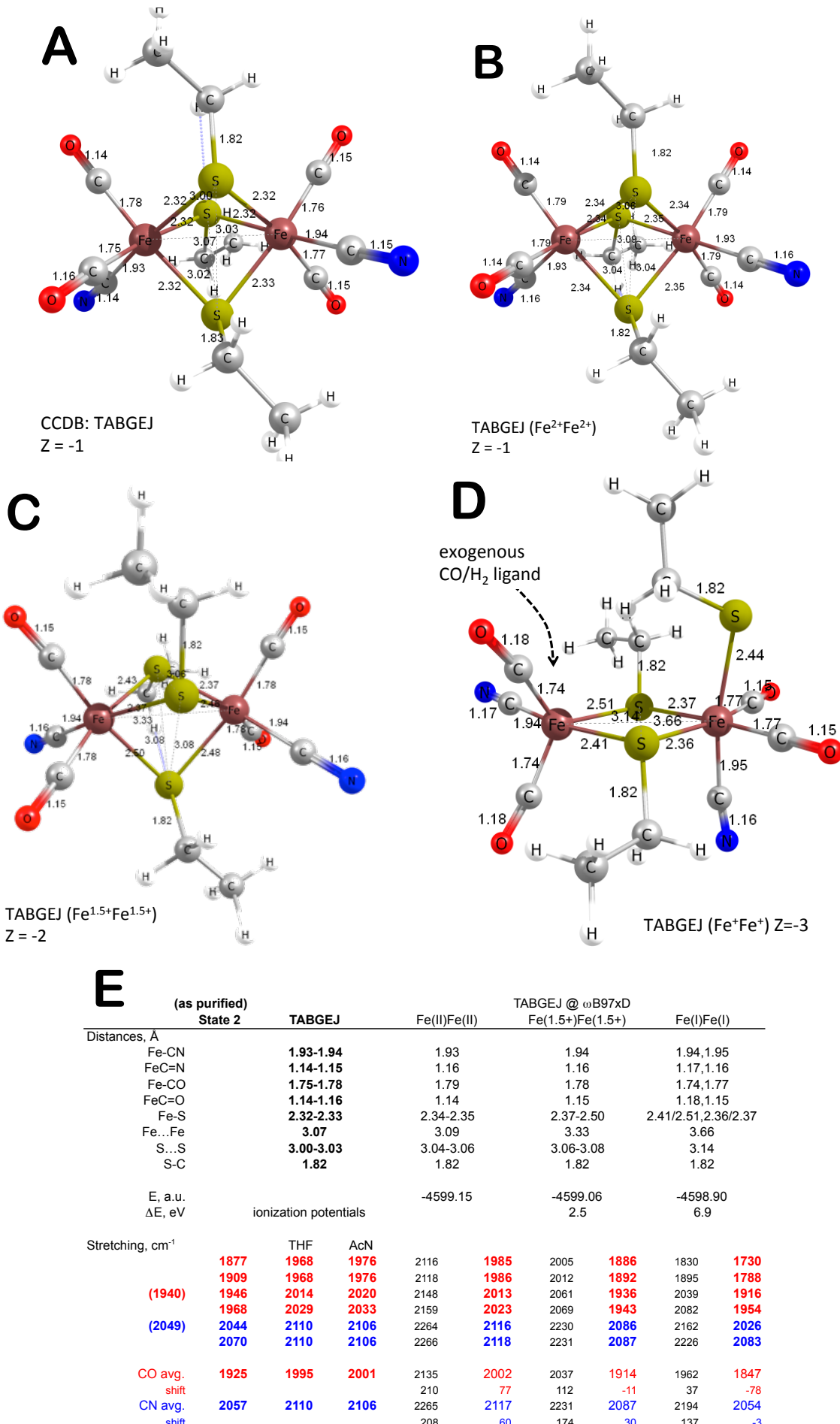


Figure S9.1: Optimized structures (at $\omega\text{B97X-D/def2TZVP}$ level) for oxidized $[\text{Fe}(\text{II})\text{Fe}(\text{II})]$ (A: X-ray B: calculated), one $[\text{Fe}(\text{I})\text{Fe}(\text{II})]^-$ (C), and two-electron reduced $[\text{Fe}(\text{I})\text{Fe}(\text{I})]^{2-}$ (D) **Model D-Cys**, $[\text{Fe}]_2$ cluster model binding via a protein derived cysteine ligand and (E) calculated intramolecular distances and scaled diatomic stretching frequencies in comparison to the experimental HydF^{EG} and TABGEJ (Ref. ¹⁰) bands.

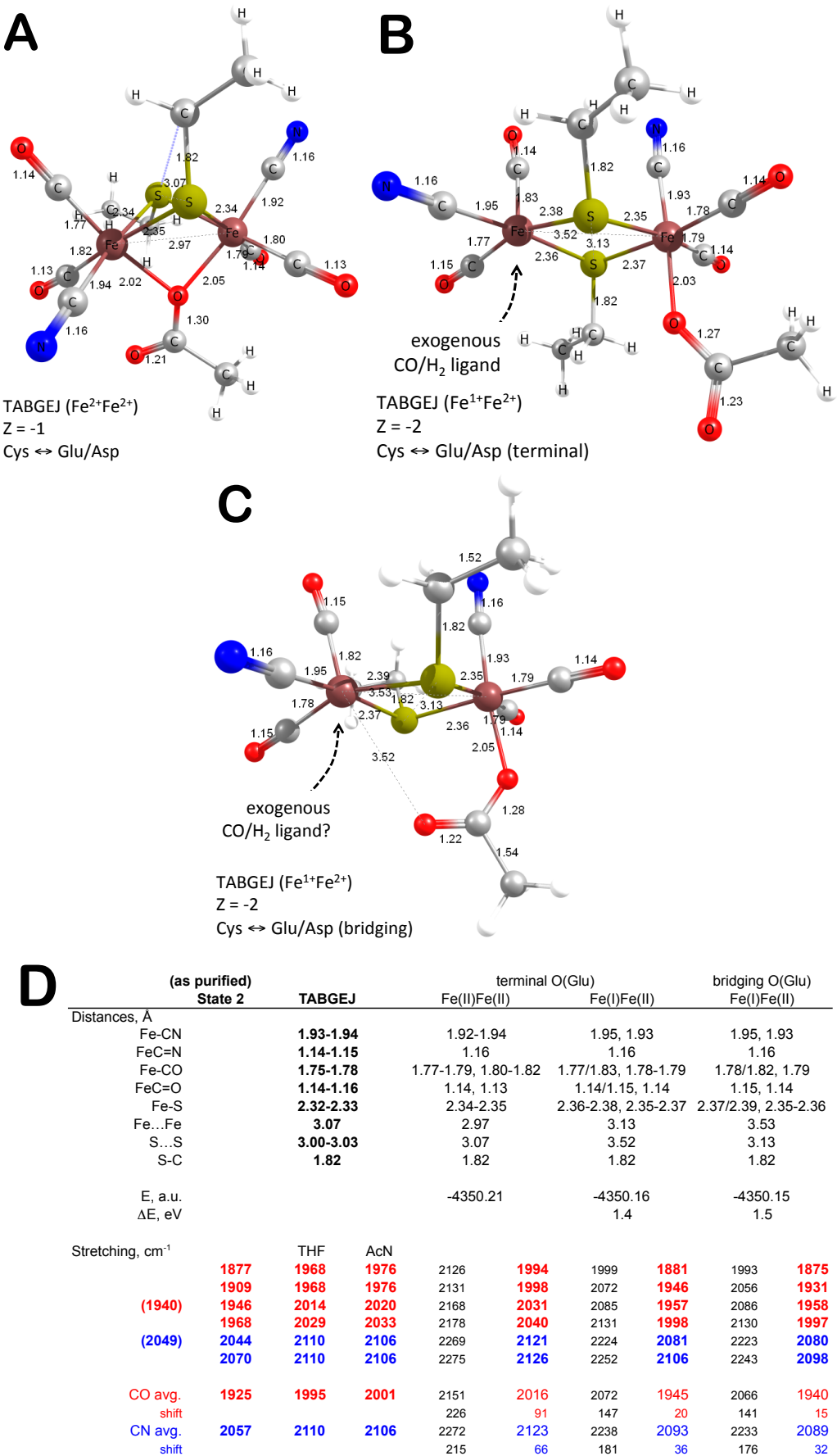


Figure S9.2: Optimized structures (at $\omega\text{B97X-D/def2TZVP}$ level) for oxidized $[\text{Fe}^{(\text{II})}\text{Fe}^{(\text{II})}]$ (A: X-ray B: calculated) and reduced $[\text{Fe}^{(\text{I})}\text{Fe}^{(\text{II})}]^-$ (C) **Model D-Glu/Asp**, $[\text{Fe}]_2$ cluster model binding via a protein derived glutamate/aspartate ligand and (D) calculated intramolecular distances and scaled diatomic stretching frequencies (in comparison to the experimental HydF^{EG} and TABGEJ (Ref. ¹⁰) bands

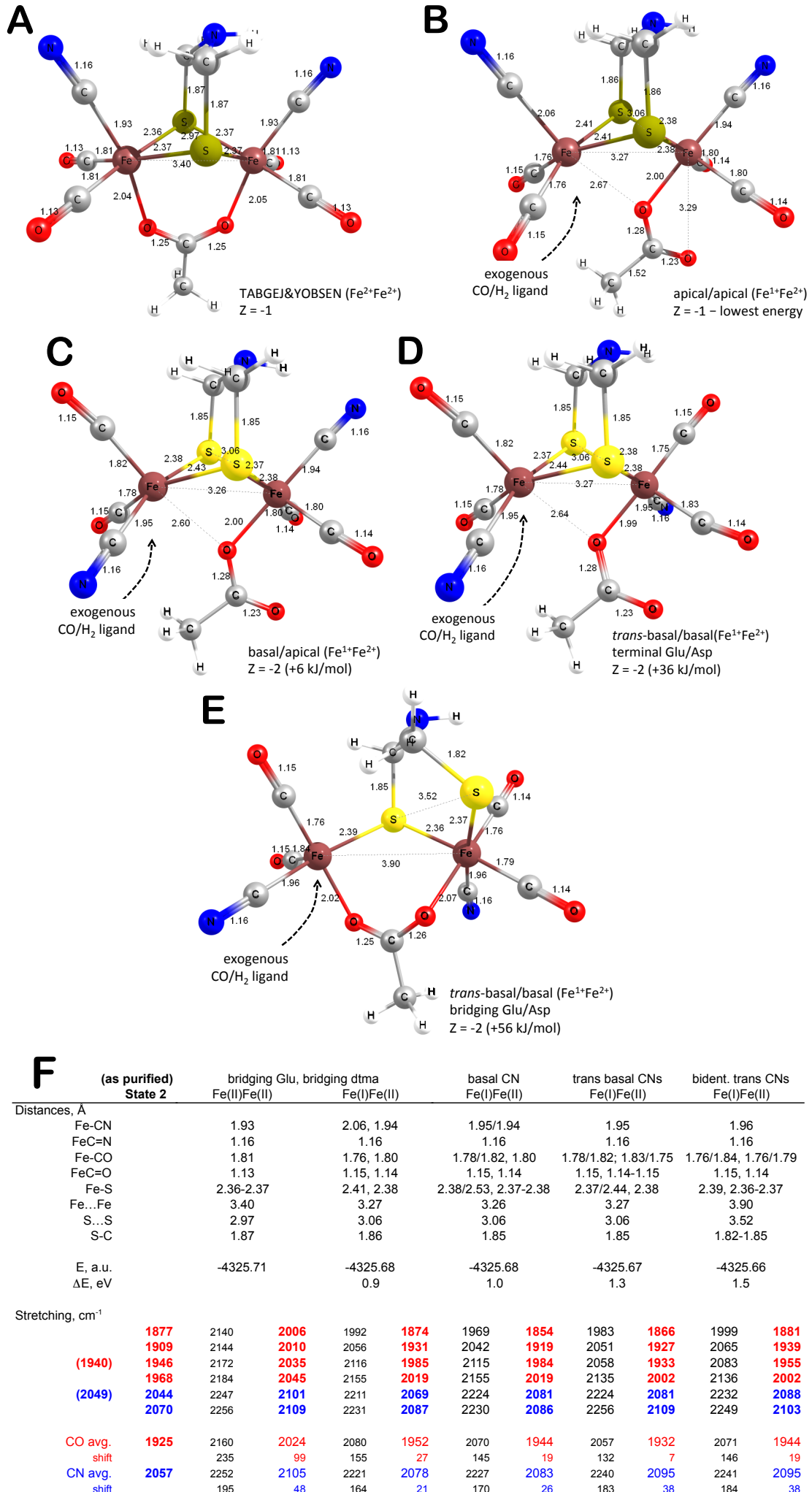


Figure S9.3: Optimized structures (at $\omega\text{B97X-D/def2TZVP}$ level) for oxidized $[\text{Fe}^{(\text{II})}\text{Fe}^{(\text{II})}]$ (A) and reduced $[\text{Fe}^{(\text{I})}\text{Fe}^{(\text{II})}]^-$ (B-D) **Model D-Glu/Asp+DTMA** (fused structure of TABGEJ and YOBSEN complexes), $[\text{Fe}]_F$ cluster model binding via a protein derived glutamate/aspartate ligand and (F) calculated intramolecular distances and scaled diatomic stretching frequencies in comparison to the experimental HydF^{EG} bands.

10. Geometric, Energetic, and Vibrational Analyses of Models E

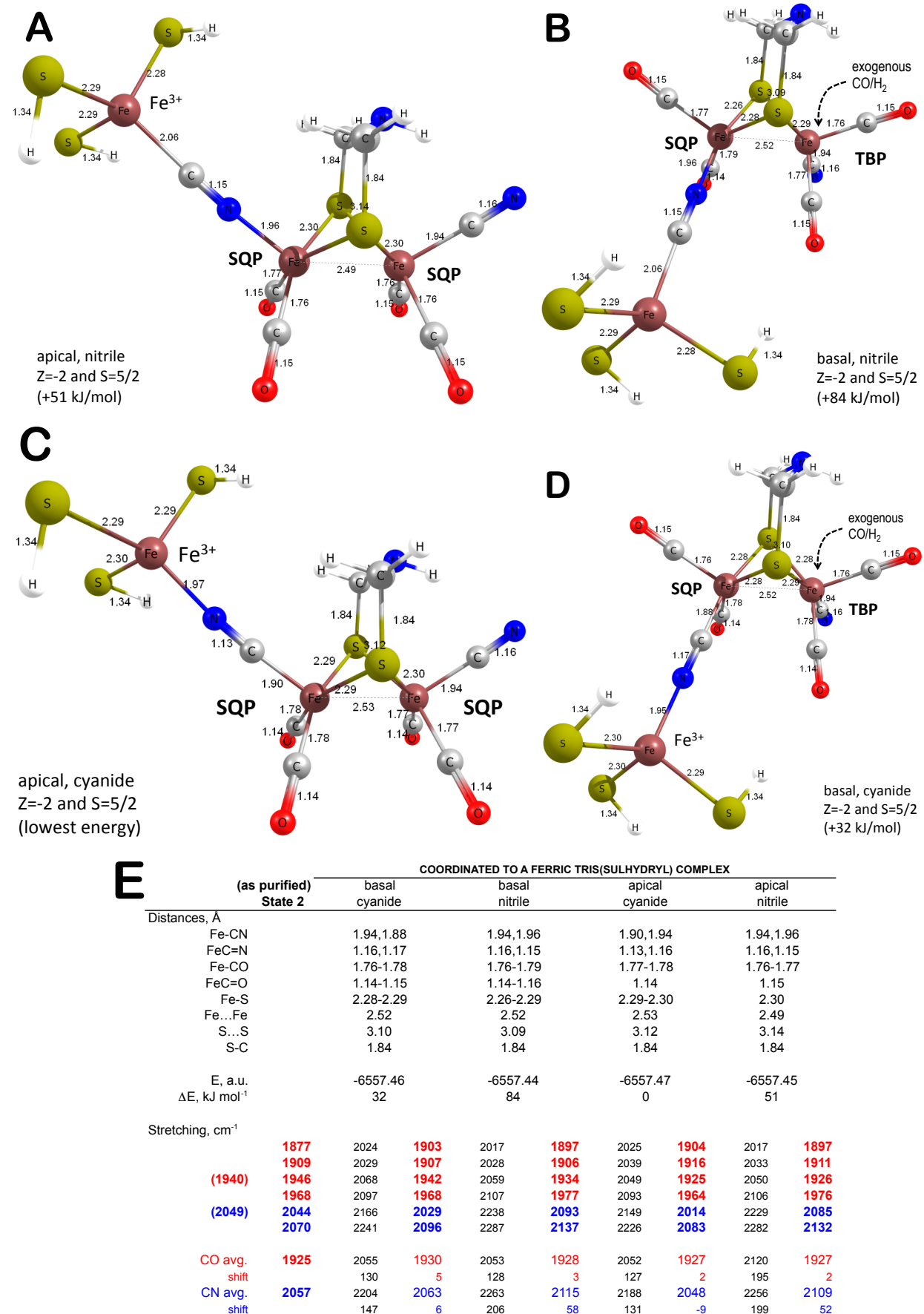


Figure S10.1: Optimized structures (at ω B97X-D/def2TZVP level) for oxidized $[\text{Fe}^{3+}] \times [\text{Fe}^{(I)}\text{Fe}^{(I)}]^{2-}$ (A-D) **Model E**, $[2\text{Fe}]_F$ cluster model binding via a bridging cyanide ligand to a ‘unique Fe site’ (modeled by $[\text{Fe}^{3+}(\text{SH})_3]$) and (E) calculated intramolecular distances and scaled diatomic stretching frequencies in comparison to the experimental HydFEG bands.

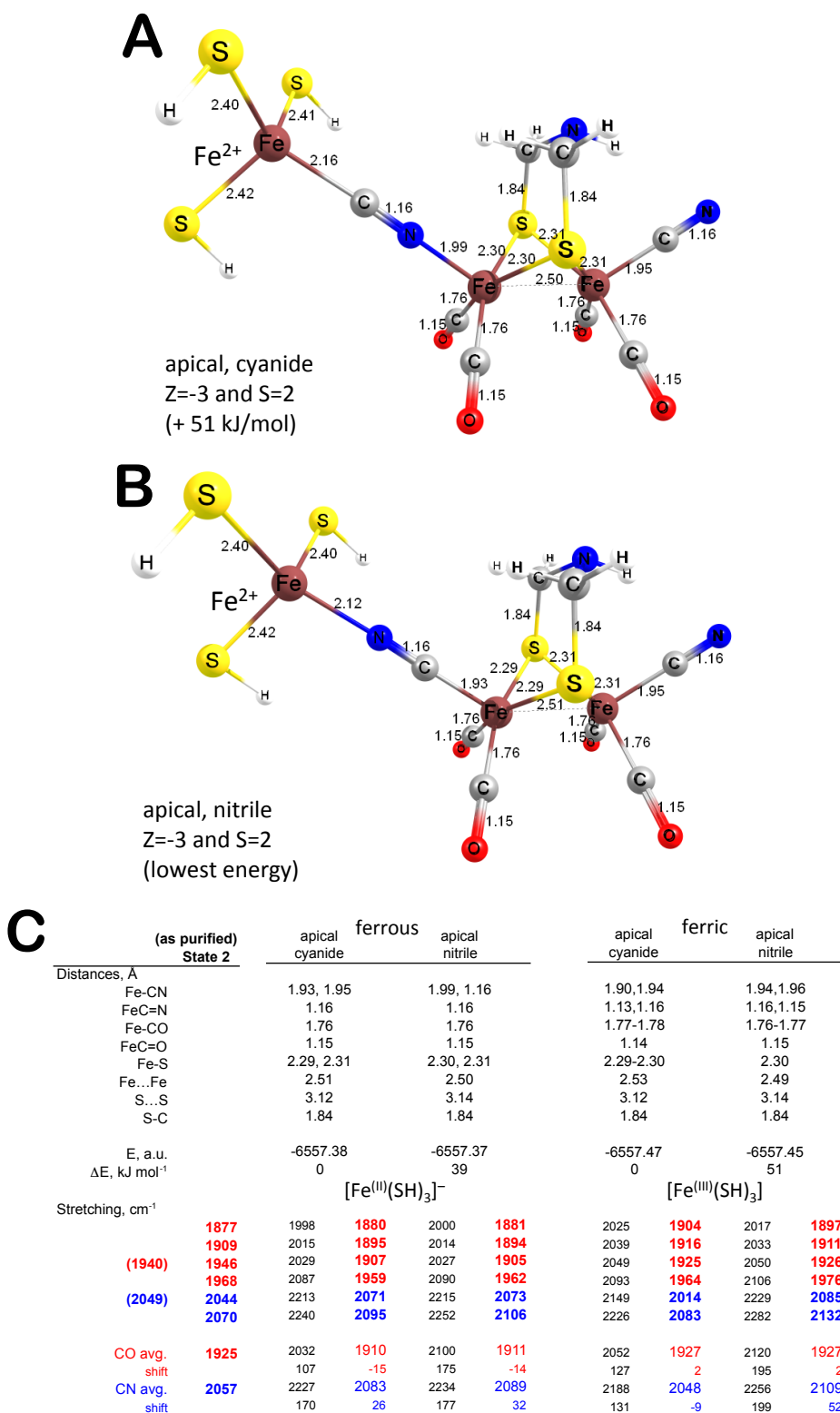


Figure S10.2: Optimized structures (at ω B97X-D/def2TZVP level) for reduced $[Fe^{2+}] \times [Fe^{(I)}Fe^{(I)}]^{2-}$ (A-B) **Model E**, $[2Fe]_F$ cluster model binding via a bridging cyanide ligand to a ‘unique Fe site’ (modeled by $[Fe^{2+}(SH)_3]^-$) and (C) calculated intramolecular distances and scaled diatomic stretching frequencies in comparison to the experimental HydF^{EG} bands and the one-electron oxidized form.

11. Geometric, Energetic, and Vibrational Analyses of Models F

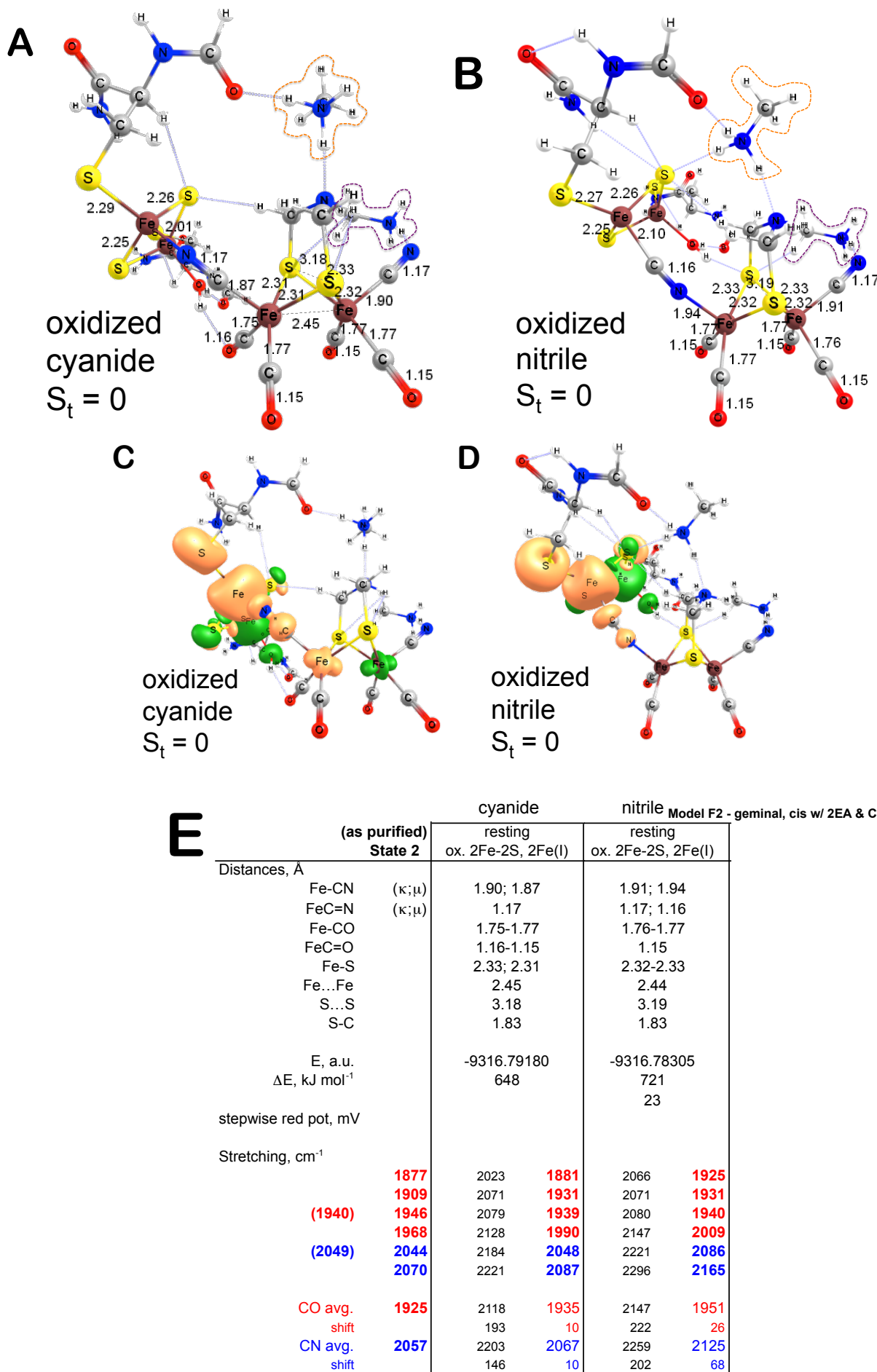


Figure S11.1: Optimized structures (at ω B97X-D/SVP level) for oxidized, vicinal, *cis* ($\text{Cys}_2[2\text{Fe}-2\text{S}] \times [\text{Fe}^{(\text{I})}\text{Fe}^{(\text{I})}]^{2-}$) (A-B) **Model F**, $[2\text{Fe}]_F$ cluster model binding *via* a bridging cyanide ligand in two arrangements from HydA with frozen backbone atoms. A water molecule completes the distal Fe coordination environment of the $[2\text{Fe}-2\text{S}]$ cluster. Atomic spin density contour plots at $0.003 e^- \text{\AA}^{-3}$ contour level (C-D). Calculated intramolecular distances and scaled diatomic stretching frequencies (E) in comparison to the experimental HydF^{EG} bands.

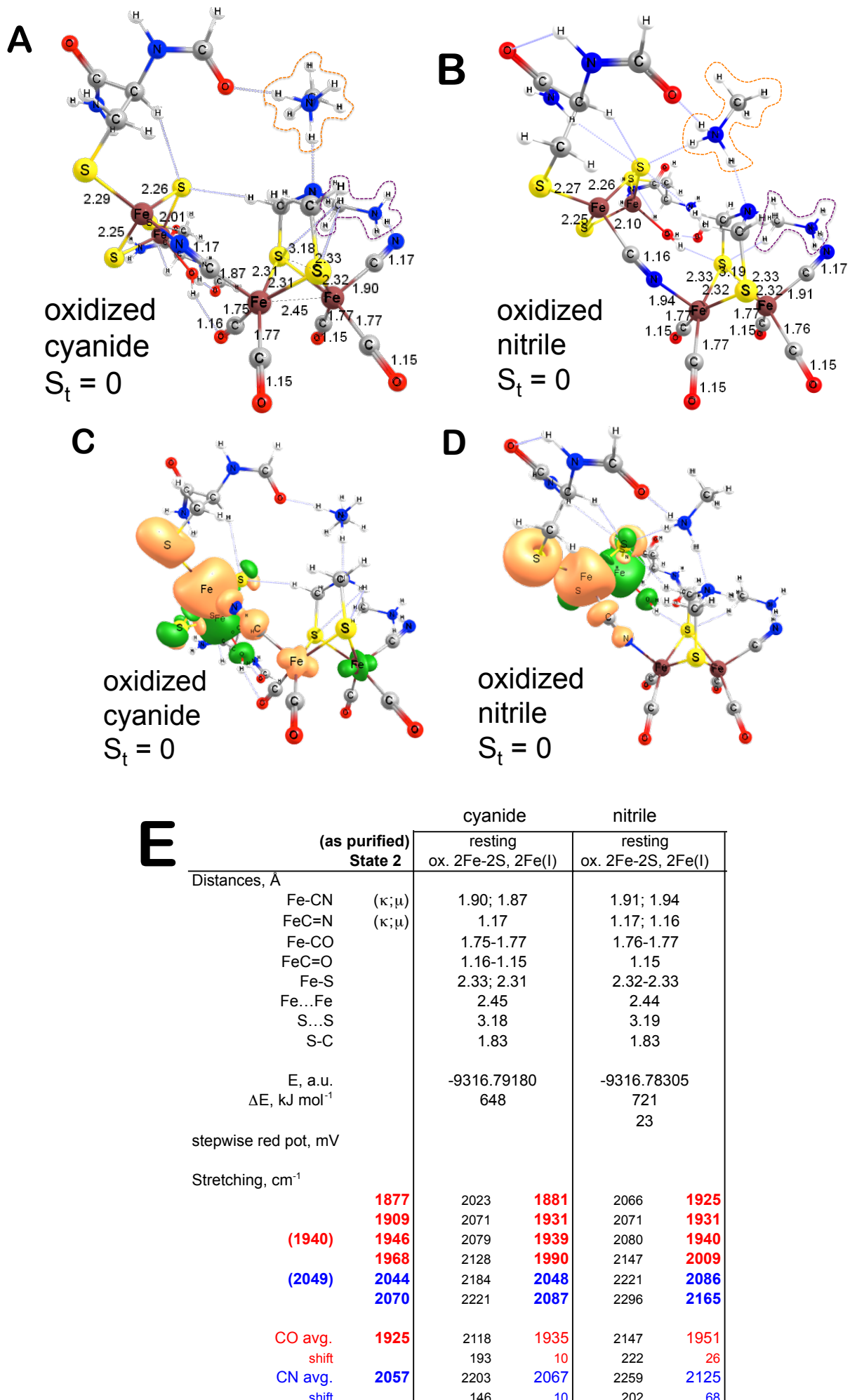


Figure S11.2: Optimized structures (at ω B97X-D/SVP level) for reduced vicinal, *cis* ($\text{Cys}_2[2\text{Fe}-2\text{S}]^-\times[\text{Fe}^{(\text{I})}\text{Fe}^{(\text{I})}]^{2-}$) (A-B) **Model F**, $[\text{Fe}]_F$ cluster model binding *via* a bridging cyanide ligand in two arrangements from HydA with frozen backbone atoms. A water molecule completes the distal Fe coordination environment of the $[2\text{Fe}-2\text{S}]$ cluster. Atomic spin density contour plots at $0.003 e^- \text{\AA}^{-3}$ contour level (C-D). Calculated intramolecular distances and scaled diatomic stretching frequencies (E) in comparison to the experimental HydF^{EG} bands.

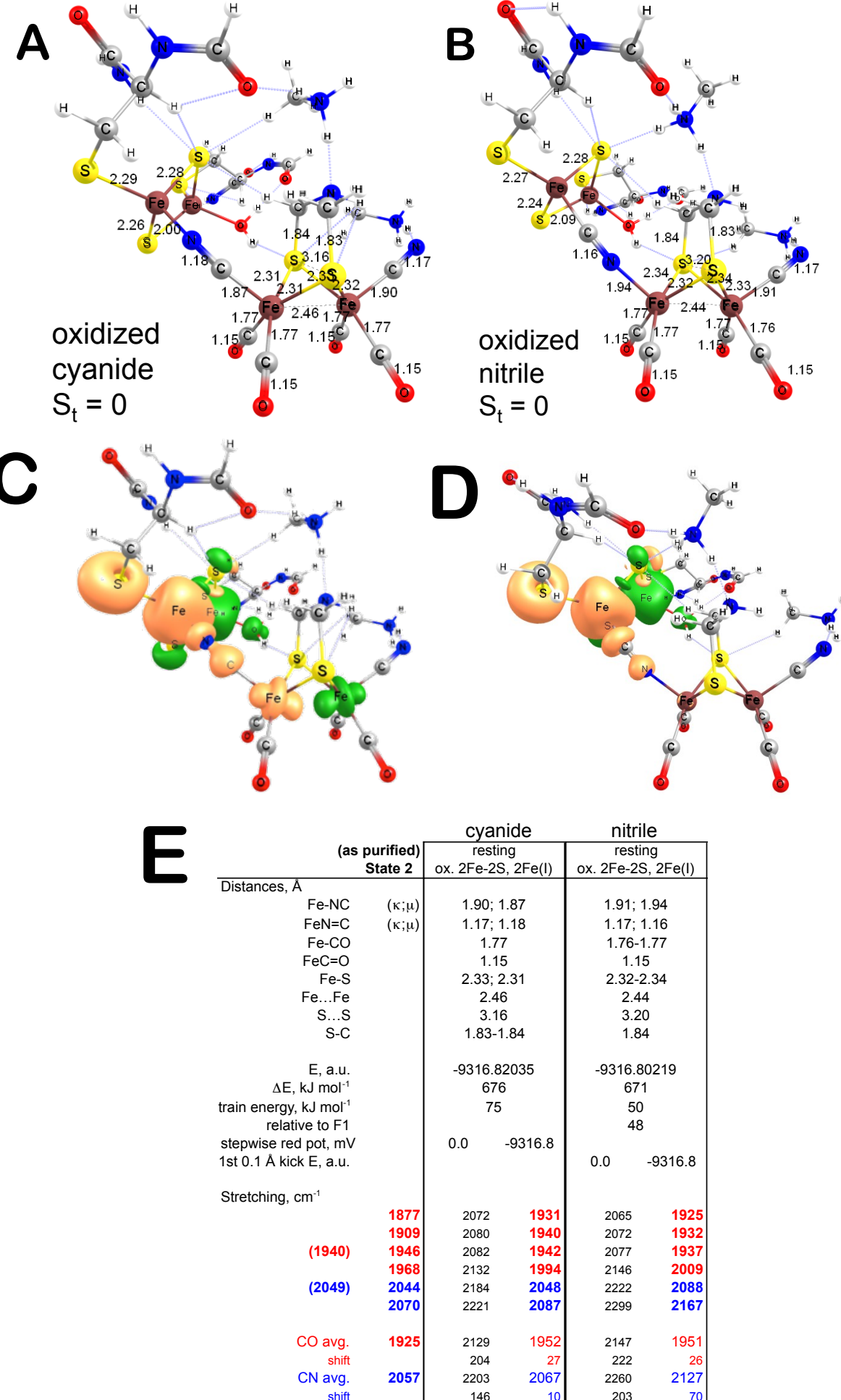


Figure S11.3: Optimized structures (at ω B97X-D/SVP level) for oxidized, vicinal, *cis* ($\text{Cys}_2[2\text{Fe}-2\text{S}] \times [\text{Fe}^{(\text{I})}\text{Fe}^{(\text{I})}]^{2-}$) (A-B) **Model F**, $[2\text{Fe}]_F$ cluster model binding *via* a bridging cyanide ligand in two arrangements from HydA without any constraints on atomic positions. A water molecule completes the distal Fe coordination environment of the $[2\text{Fe}-2\text{S}]$ cluster. Atomic spin density contour plots at $0.003 e^- \text{\AA}^{-3}$ contour level (C-D). Calculated intramolecular distances and scaled diatomic stretching frequencies (E) in comparison to the experimental HydF^{EG} bands.

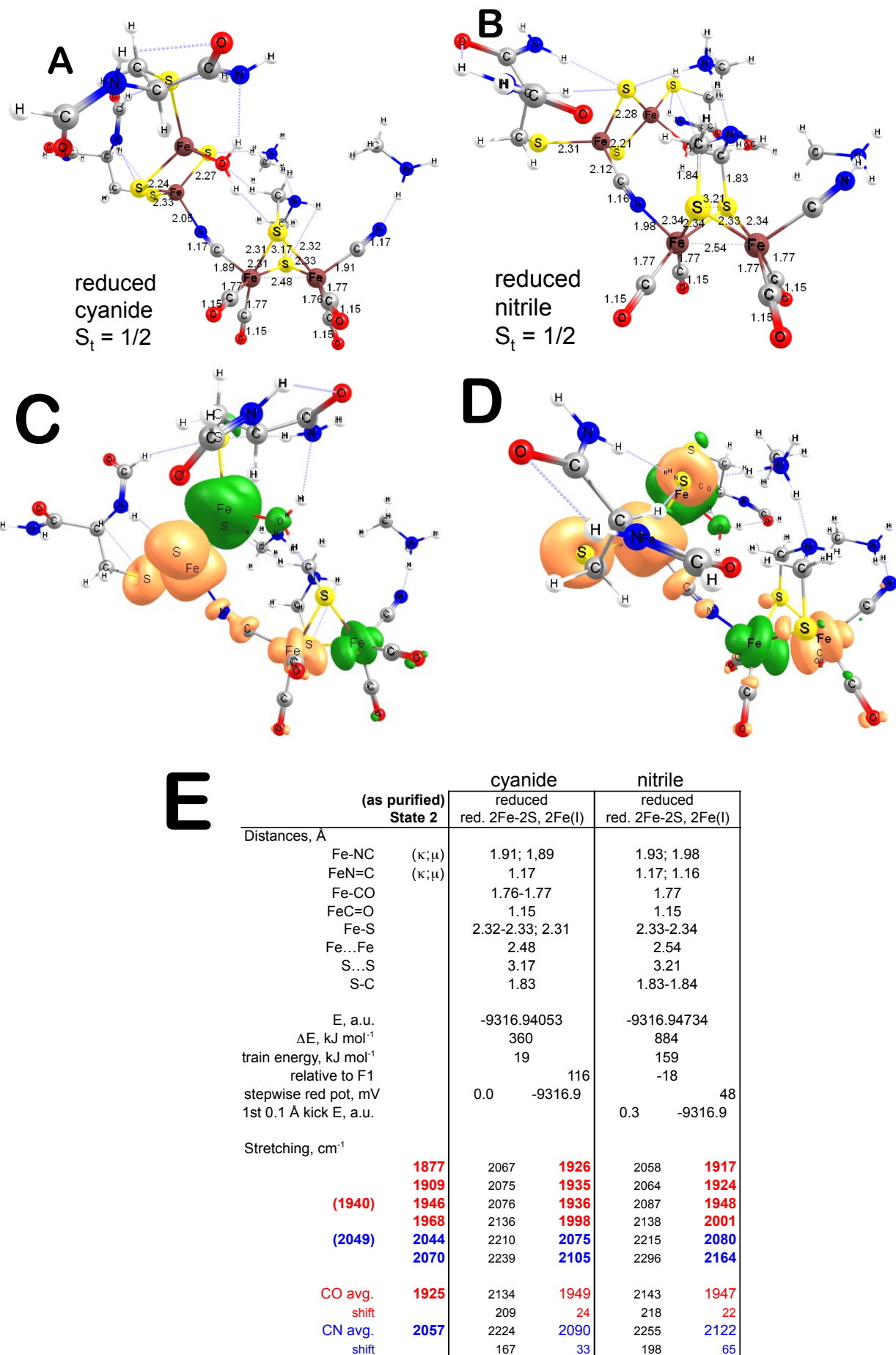


Figure S11.4: Optimized structures (at ω B97X-D/SVP level) for reduced vicinal, *cis* ($\text{Cys}_2[2\text{Fe}-2\text{S}]^-\times[\text{Fe}^{(\text{I})}\text{Fe}^{(\text{I})}]^{2-}$ (A-B) **Model F**, $[\text{Fe}]_F$ cluster model binding *via* a bridging cyanide ligand in two arrangements from HydA without any constraints on atomic positions. A water molecule completes the distal Fe coordination environment of the $[2\text{Fe}-2\text{S}]$ cluster. Atomic spin density contour plots at $0.003 e^- \text{\AA}^{-3}$ contour level (C-D). Calculated intramolecular distances and scaled diatomic stretching frequencies (E) in comparison to the experimental HydFEG bands.

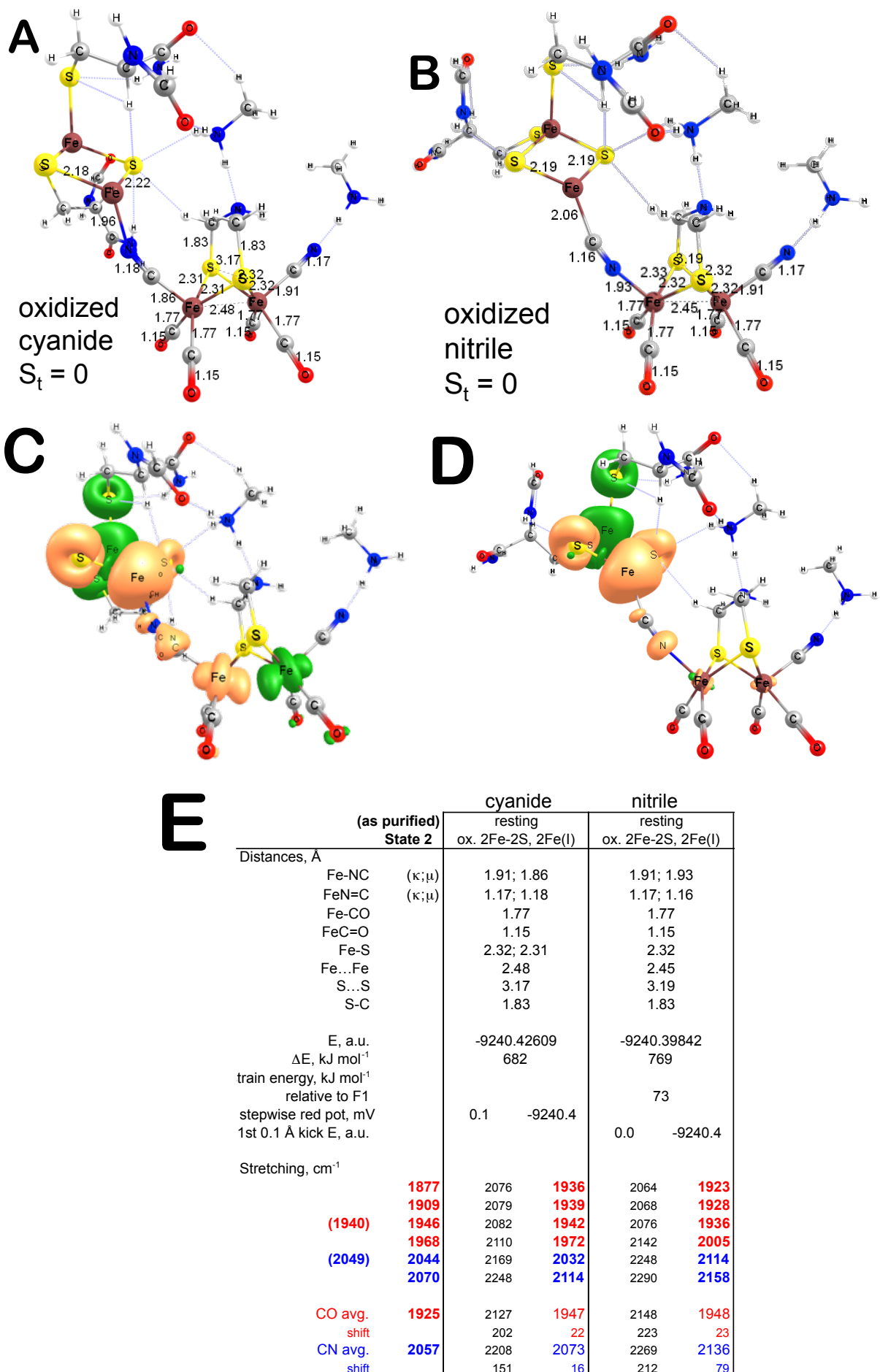


Figure S11.5: Optimized structures (at ω B97X-D/SVP level) for oxidized, geminal $(\text{Cys})_2[2\text{Fe}-2\text{S}] \times [\text{Fe}^{(\text{I})}\text{Fe}^{(\text{I})}]^{2-}$ (A-B) **Model F**, $[2\text{Fe}]_{\text{F}}$ cluster model binding via a bridging cyanide ligand in two arrangements from HydA without any constraints on atomic positions. Atomic spin density contour plots at $0.003 e^{-} \text{Å}^{-3}$ contour level (C-D). Calculated intramolecular distances and scaled diatomic stretching frequencies (E) in comparison to the experimental HydF^{EG} bands.

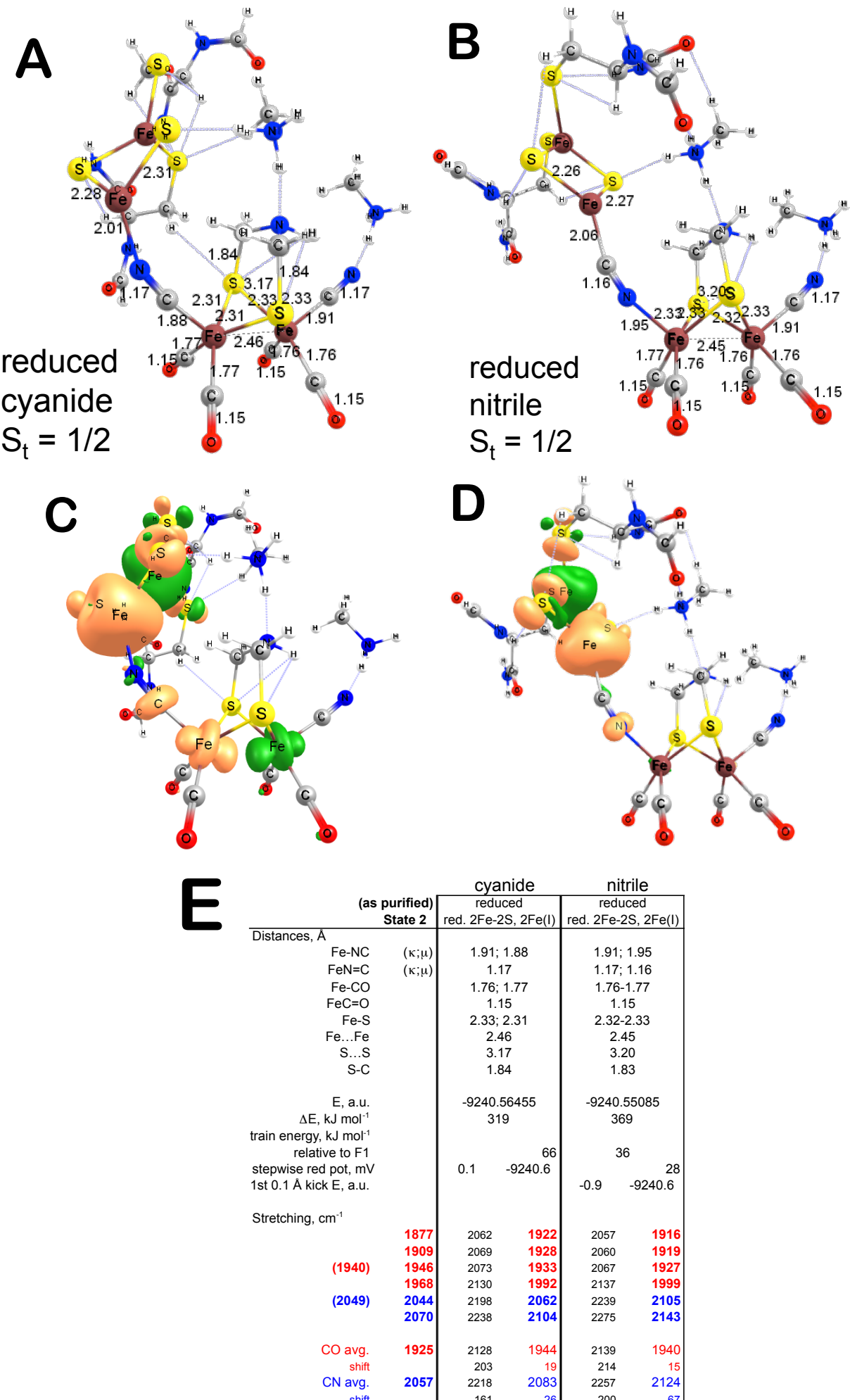


Figure S11.6: Optimized structures (at ω B97X-D/SVP level) for reduced geminal ($\text{Cys}_2[2\text{Fe}-2\text{S}]^-\times[\text{Fe}^{(\text{I})}\text{Fe}^{(\text{I})}]^{2-}$) (A-B) **Model F**, $[\text{Fe}]_F$ cluster model binding via a bridging cyanide ligand in two arrangements from HydA without any constraints on atomic positions. A water molecule completes the distal Fe coordination environment of the $[2\text{Fe}-2\text{S}]$ cluster. Atomic spin density contour plots at $0.003 e^- \text{\AA}^{-3}$ contour level (C-D). Calculated intramolecular distances and scaled diatomic stretching frequencies (E) in comparison to the experimental HydF^{EG} bands.

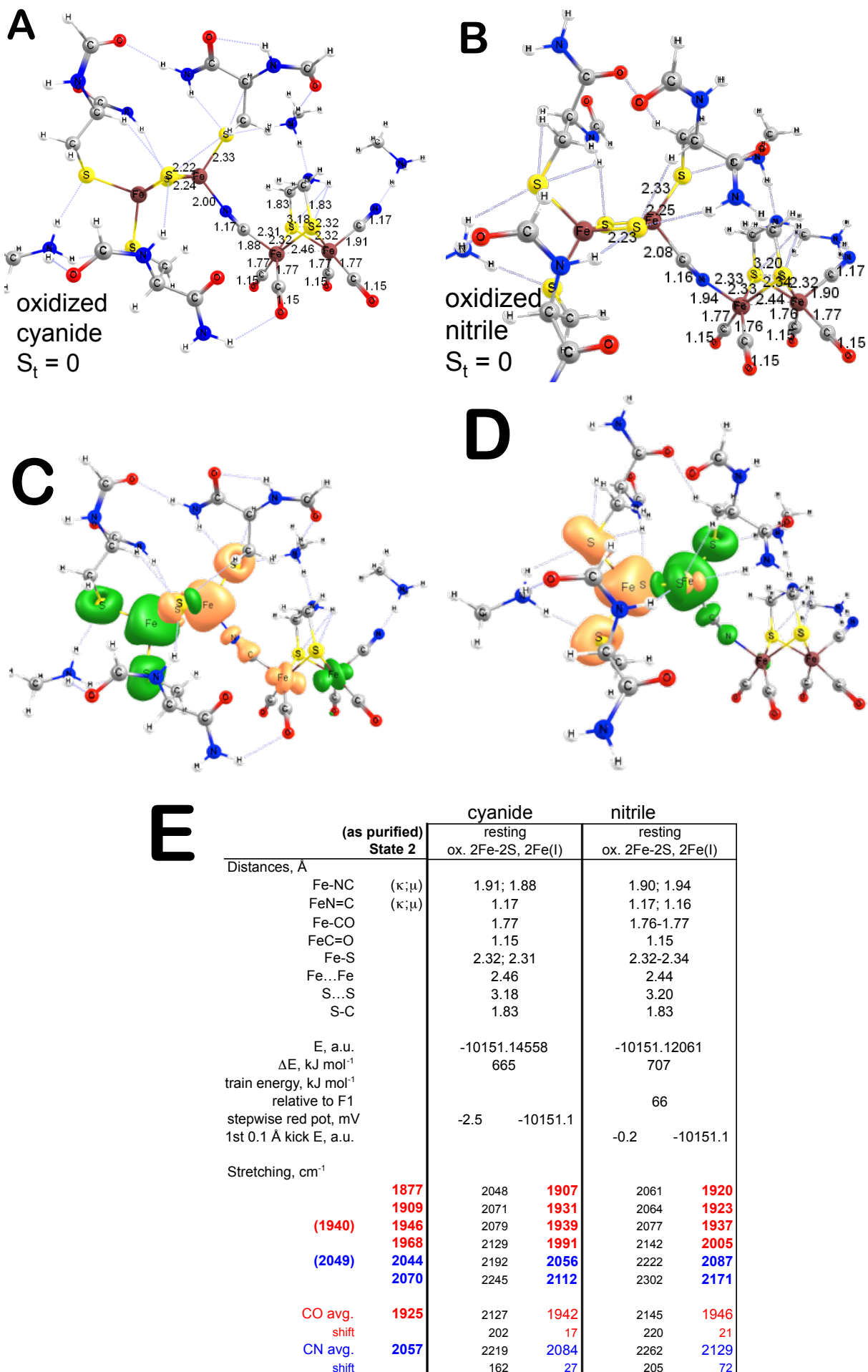


Figure S11.7: Optimized structures (at ω B97X-D/SVP level) for oxidized, $(\text{Cys})_3[2\text{Fe}-2\text{S}]^-\times[\text{Fe}^{(\text{I})}\text{Fe}^{(\text{I})}]^{2-}$ (**A-B**) **Model F**, $[\text{2Fe}]_{\text{F}}$ cluster model binding via a bridging cyanide ligand in two arrangements from HydA without any constraints on atomic positions. Atomic spin density contour plots at $0.003 e^- \text{\AA}^{-3}$ contour level (**C-D**). Calculated intramolecular distances and scaled diatomic stretching frequencies (**E**) in comparison to the experimental HydFEG bands.

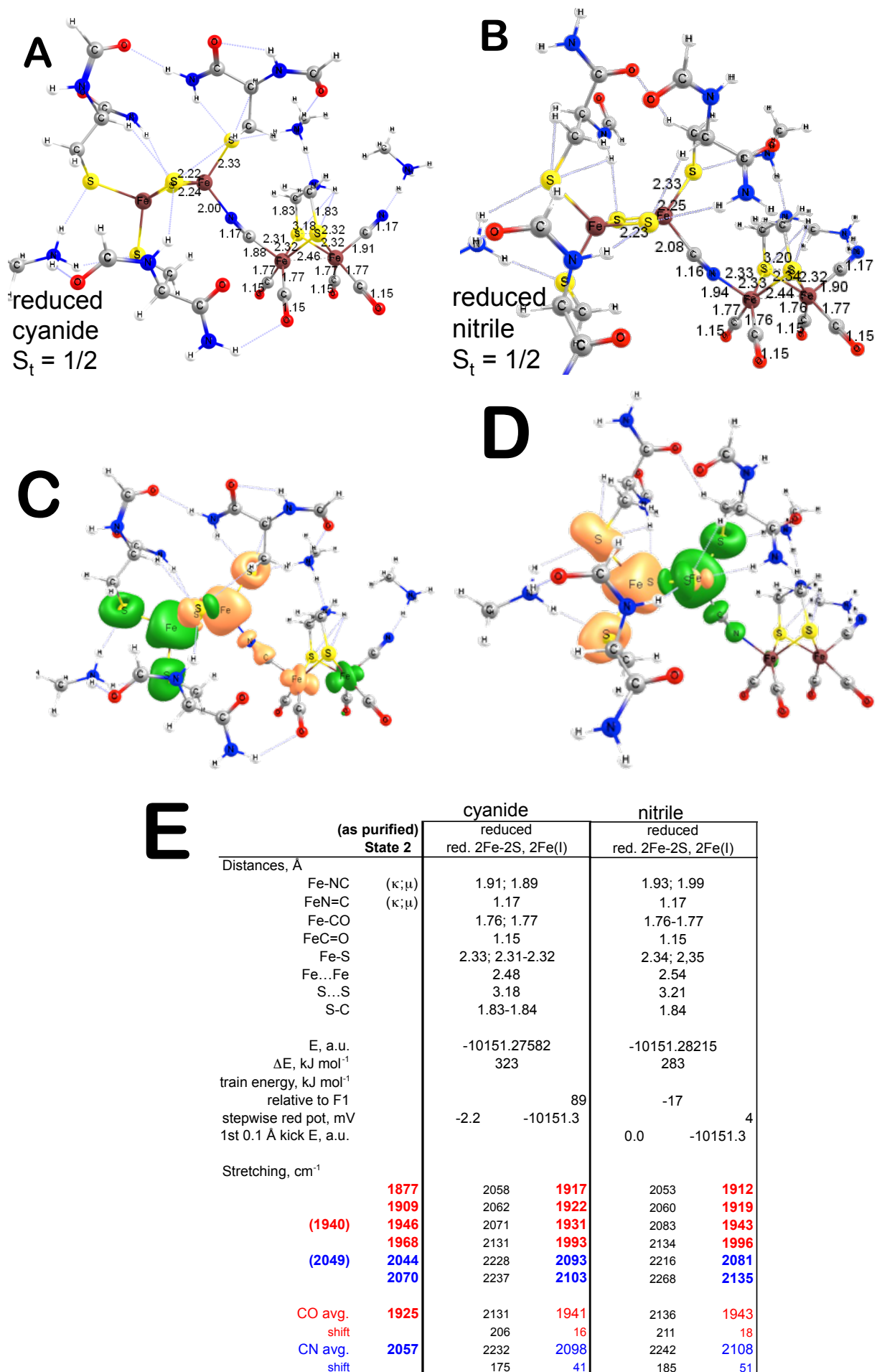


Figure S11.8: Optimized structures (at ω B97X-D/SVP level) for reduced ($\text{Cys}_3[2\text{Fe}-2\text{S}]^2-$ $\times[\text{Fe}^{(\text{I})}\text{Fe}^{(\text{I})}]^{2-}$ (A-B) **Model F**, [2Fe]_F cluster model binding via a bridging cyanide ligand in two arrangements from HydA without any constraints on atomic positions. Atomic spin density contour plots at $0.003 e^- \text{Å}^{-3}$ contour level (C-D). Calculated intramolecular distances and scaled diatomic stretching frequencies (E) in comparison to the experimental HydF^{EG} bands.

12. Geometric, Energetic, and Vibrational Analyses of Models G

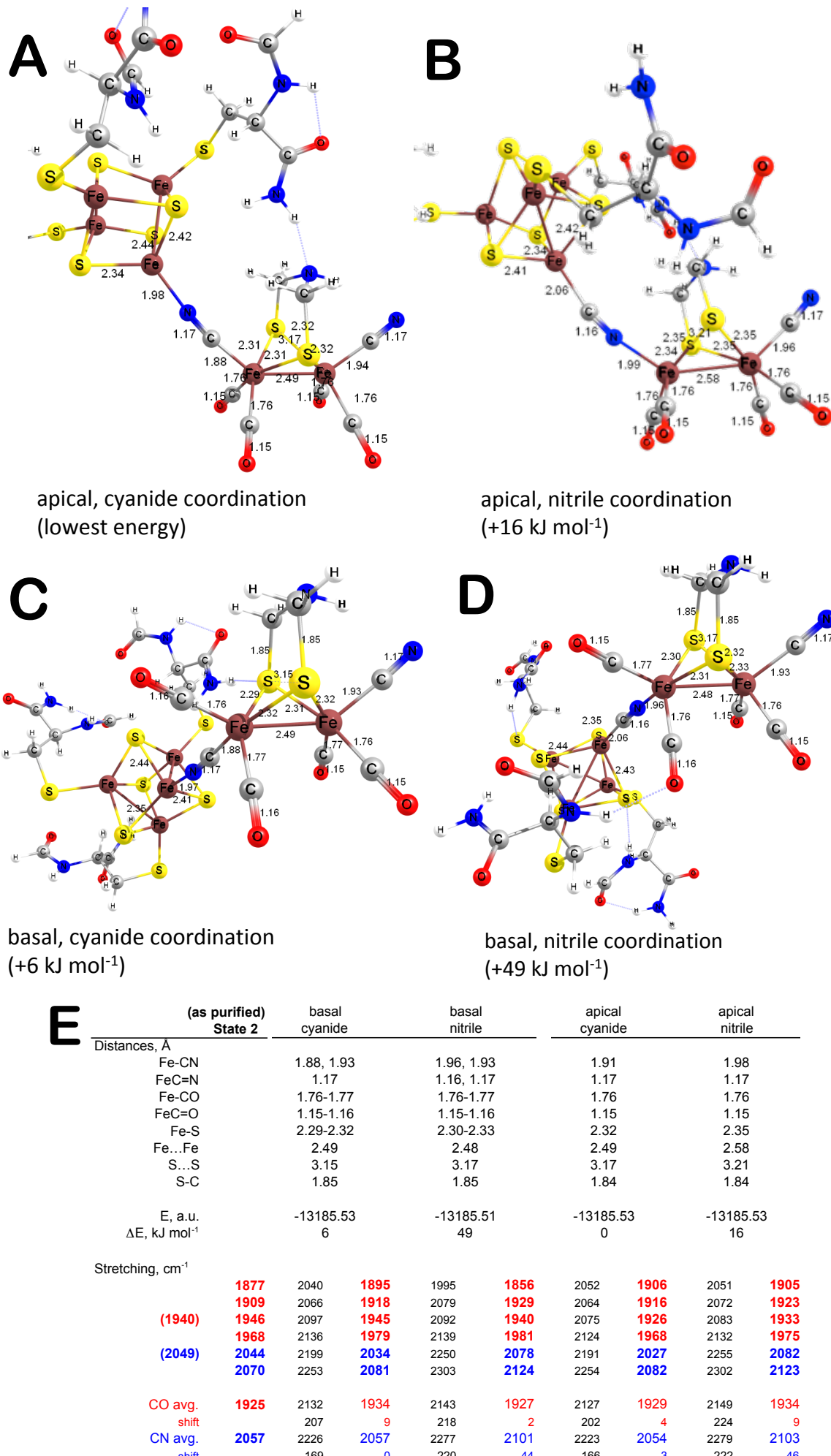


Figure S12.1: Fully optimized *in vacuo* structures (at ωB97X-D/SVP level) for [4Fe-4S]²⁺×[Fe^(I)Fe^(I)]²⁻ (A-D) **Model E**, [2Fe]_F cluster model binding via a bridging cyanide ligand to an oxidized [4Fe-4S] cluster and (E) calculated intramolecular distances and scaled diatomic stretching frequencies in comparison to the experimental HydF^{EG} bands.

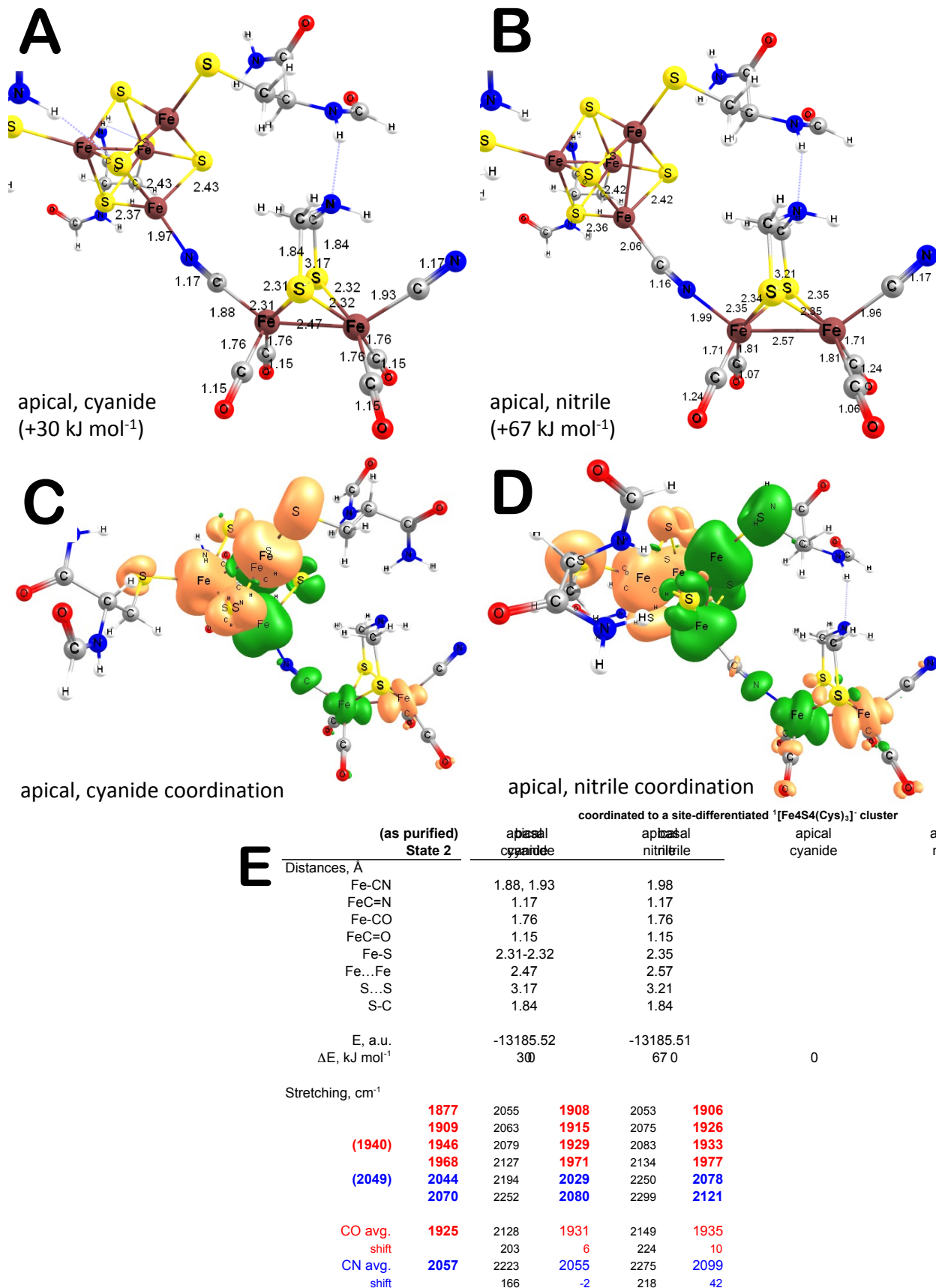


Figure S12.2: Partially optimized *in vacuo* structures (at ω B97X-D/SVP level) with constrained backbone atomic positions as in holo-HydA structure (3C8Y) for [4Fe-4S]²⁺ \times [Fe^(I)Fe^(I)]²⁻ (A-B) **Model E**, [2Fe]_F cluster model binding *via* a bridging cyanide ligand to an oxidized [4Fe-4S] cluster, (C-D) atomic spin density distribution plots (at 0.003 e⁻/Å³ contour level), and (E) calculated intramolecular distances and scaled diatomic stretching frequencies in comparison to the experimental HydF^{EG} bands (relative energies are given to the lowest energy fully optimized structure).

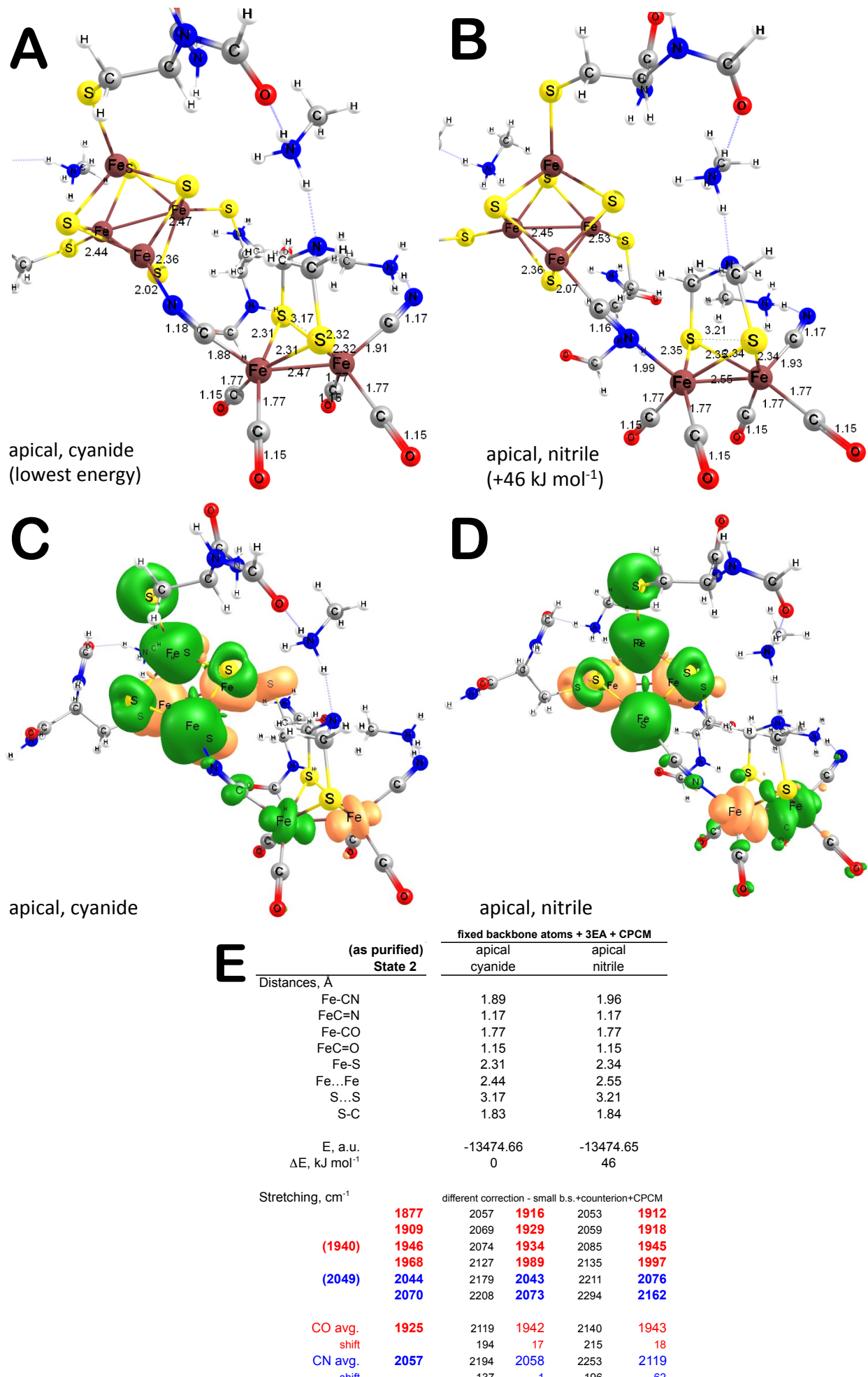


Figure S12.3: Partially optimized *in proteo* structures (at ωB97X-D/SVP level) with constrained backbone atomic positions as in holo-HydA structure (3C8Y) and in the presence of three neutralizing methylammonium counter-ions for [4Fe-4S]²⁺×[Fe^(I)Fe^(I)]²⁻ (A-B) **Model E**, [2Fe]_F cluster model binding *via* a bridging cyanide ligand to an oxidized [4Fe-4S] cluster, (C-D) atomic spin density distribution plots (at 0.003 e⁻/Å³ contour level), and (E) calculated intramolecular distances and scaled diatomic stretching frequencies in comparison to the experimental HydF^{EG} bands.

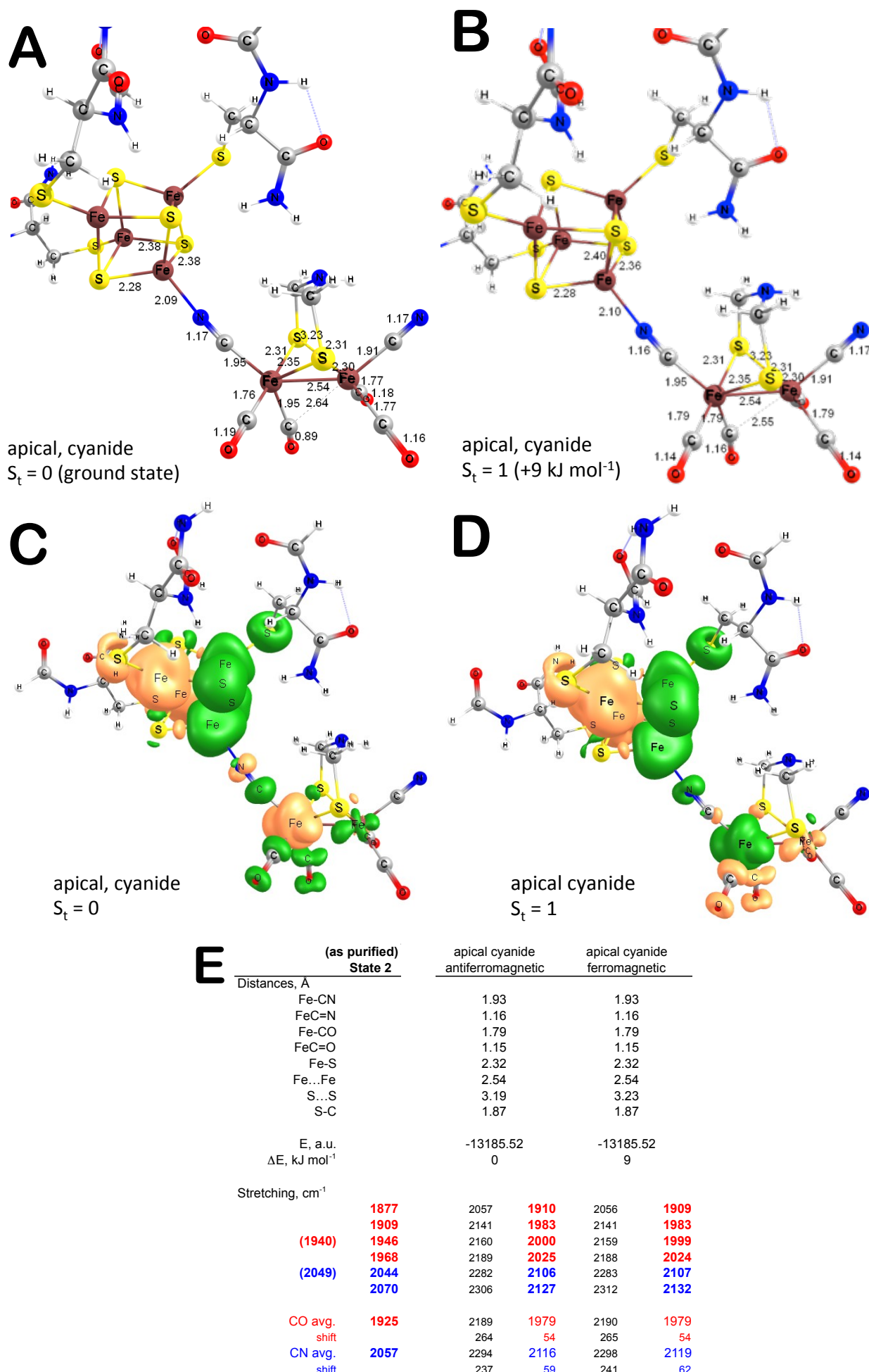


Figure S12.4: Partially optimized *in proteo* structures (at ωB97X-D/SVP level) with constrained backbone atomic positions as in holo-HydA structure (3C8Y) for [4Fe-4S]¹⁺×[Fe^(II)Fe^(I)]⁻ in open shell singlet (A) and spin-polarized triplet (B) states of **Model E**, oxidized [2Fe]_F cluster model binding *via* a bridging cyanide ligand to a reduced [4Fe-4S] cluster, (C-D) atomic spin density distribution plots (at 0.003 e⁻/Å³ contour level), and (E) calculated intramolecular distances and scaled diatomic stretching frequencies in comparison to the experimental HydF^{EG} bands.

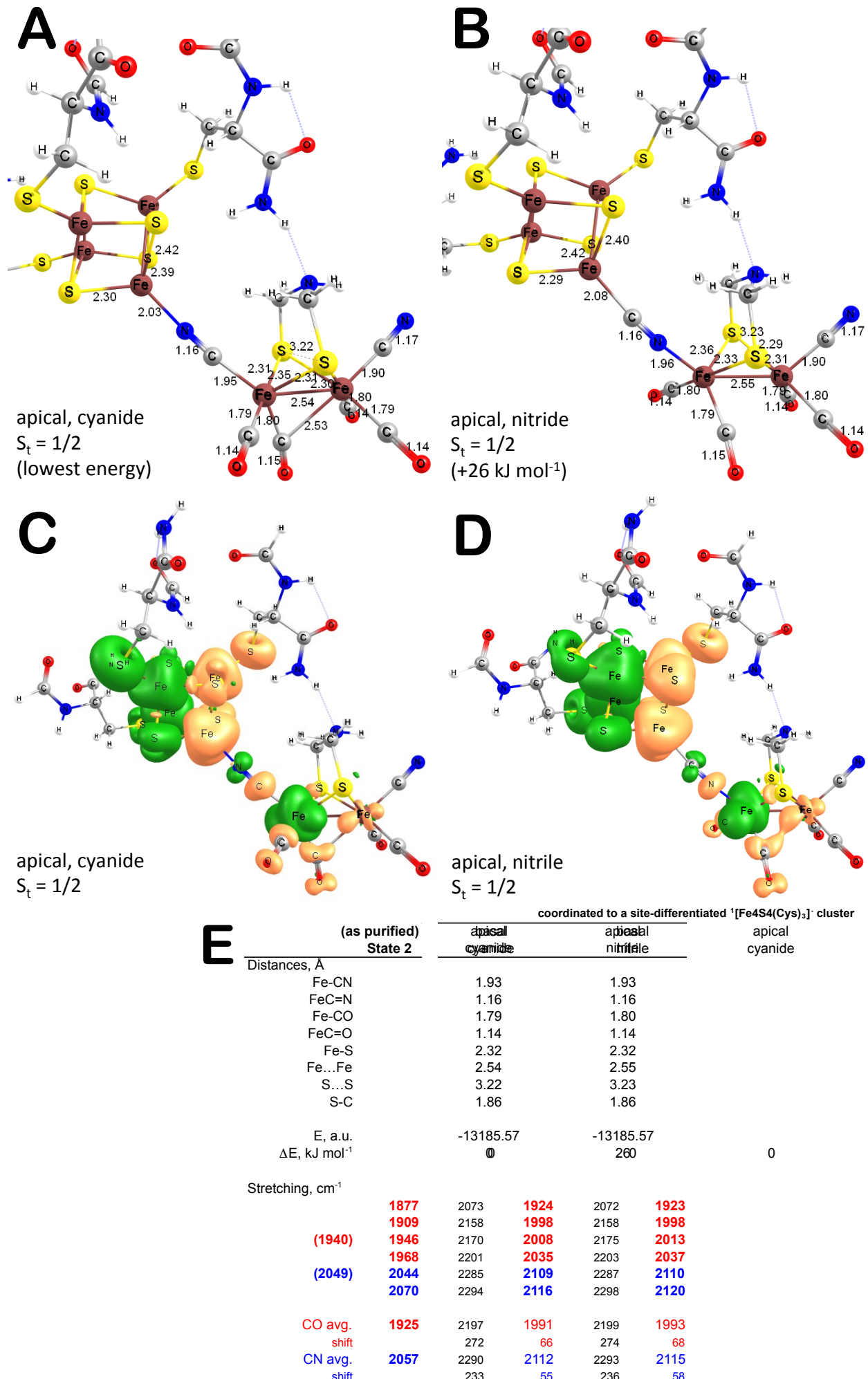


Figure S12.5: Partially optimized *in proteo* structures (at ωB97X-D/SVP level) with constrained backbone atomic positions as in holo-HydA structure (3C8Y) for [4Fe-4S]²⁺×[Fe^(II)Fe^(I)]⁻ in spin-polarized doublet state (A-B) of **Model E**, oxidized [2Fe]_F cluster model binding *via* a bridging cyanide ligand to an oxidized [4Fe-4S] cluster, (C-D) atomic spin density distribution plots (at 0.003 e⁻/Å³ contour level), and (E) calculated intramolecular distances and scaled diatomic stretching frequencies in comparison to the experimental HydF^{EG} bands.

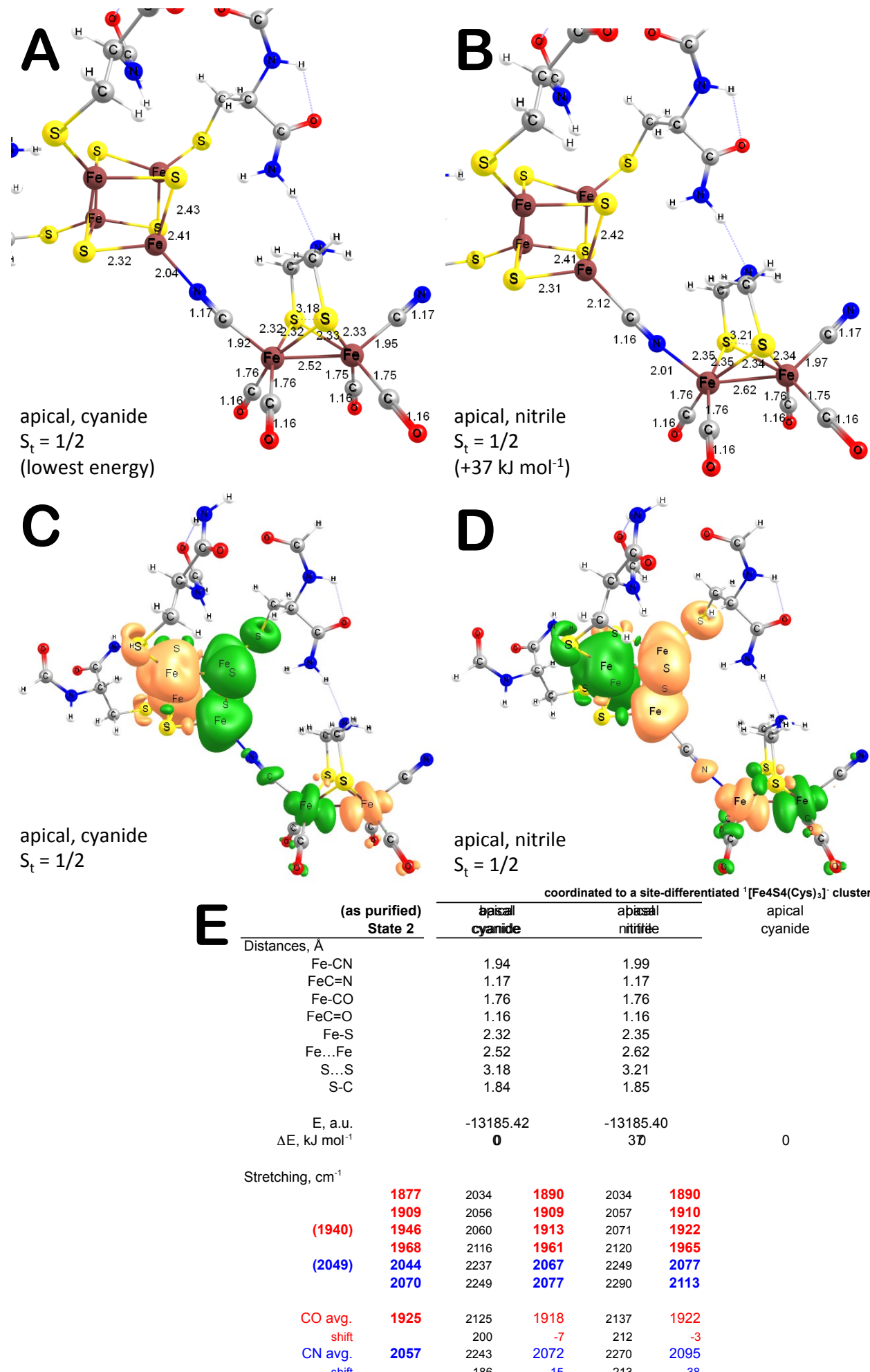


Figure S12.6: Partially optimized *in proteo* structures (at ωB97X-D/SVP level) with constrained backbone atomic positions as in holo-HydA structure (3C8Y) for [4Fe-4S]¹⁺×[Fe^(I)Fe^(I)]²⁻ in spin-polarized doublet state (A-B) of Model E, reduced [2Fe]_F cluster model binding *via* a bridging cyanide ligand to an reduced [4Fe-4S] cluster, (C-D) atomic spin density distribution plots (at 0.003 e⁻/Å³ contour level), and (E) calculated intramolecular distances and scaled diatomic stretching frequencies in comparison to the experimental HydF^{EG} bands.

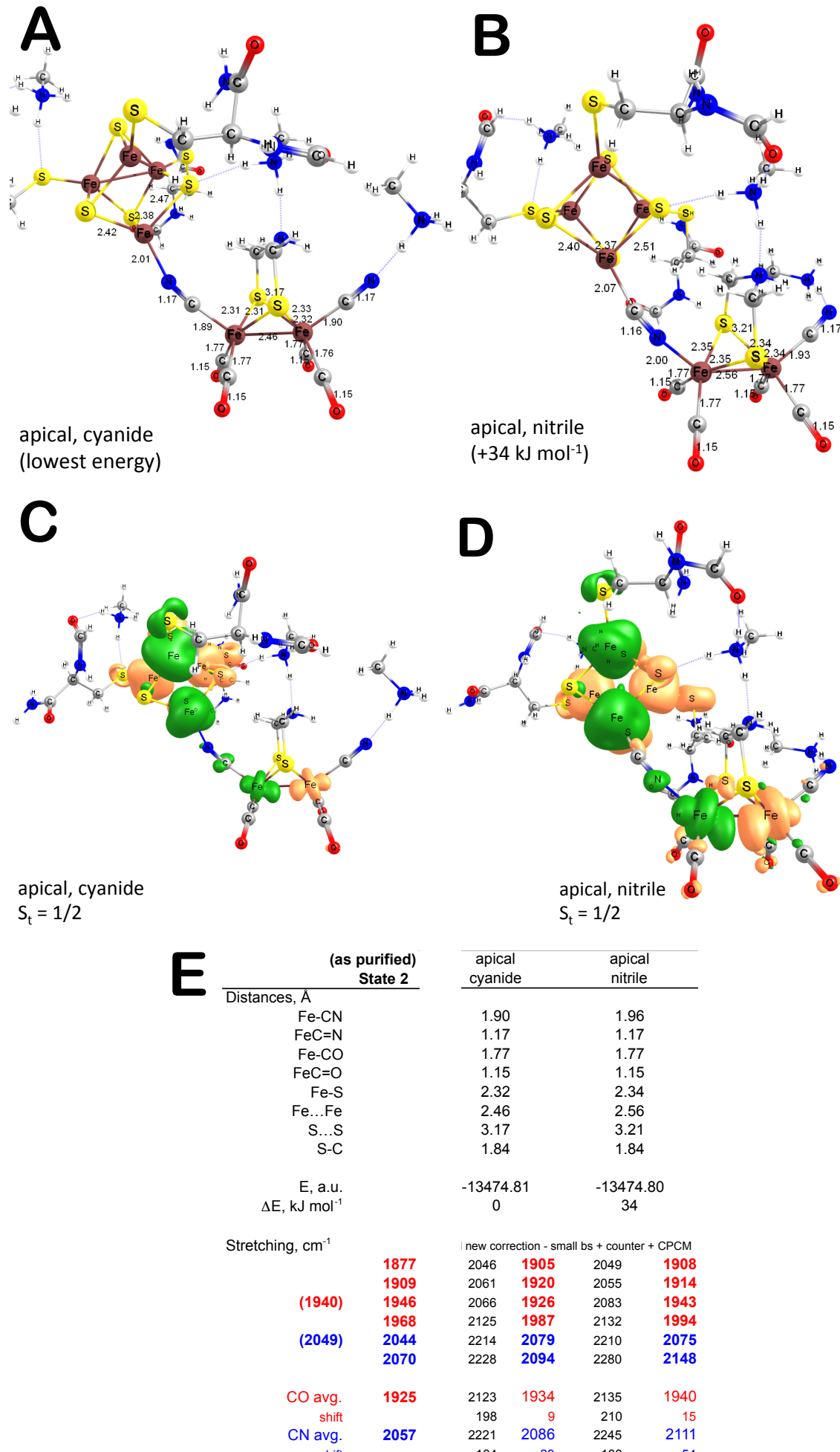


Figure S12.7: Partially optimized *in proteo* structures (at ω B97X-D/SVP level) with constrained backbone atomic positions as in holo-HydA structure (3C8Y) and in the presence of three neutralizing methylammonium counter-ions for $[4\text{Fe}-4\text{S}]^{1+} \times [\text{Fe}^{(\text{I})}\text{Fe}^{(\text{I})}]^{2-}$ (A-B) **Model E**, reduced $[2\text{Fe}]_F$ cluster model binding *via* a bridging cyanide ligand to a reduced $[4\text{Fe}-4\text{S}]$ cluster, (C-D) atomic spin density distribution plots (at 0.003 e⁻/Å³ contour level), and (E) calculated intramolecular distances and scaled diatomic stretching frequencies in comparison to the experimental HydF^{EG} bands.

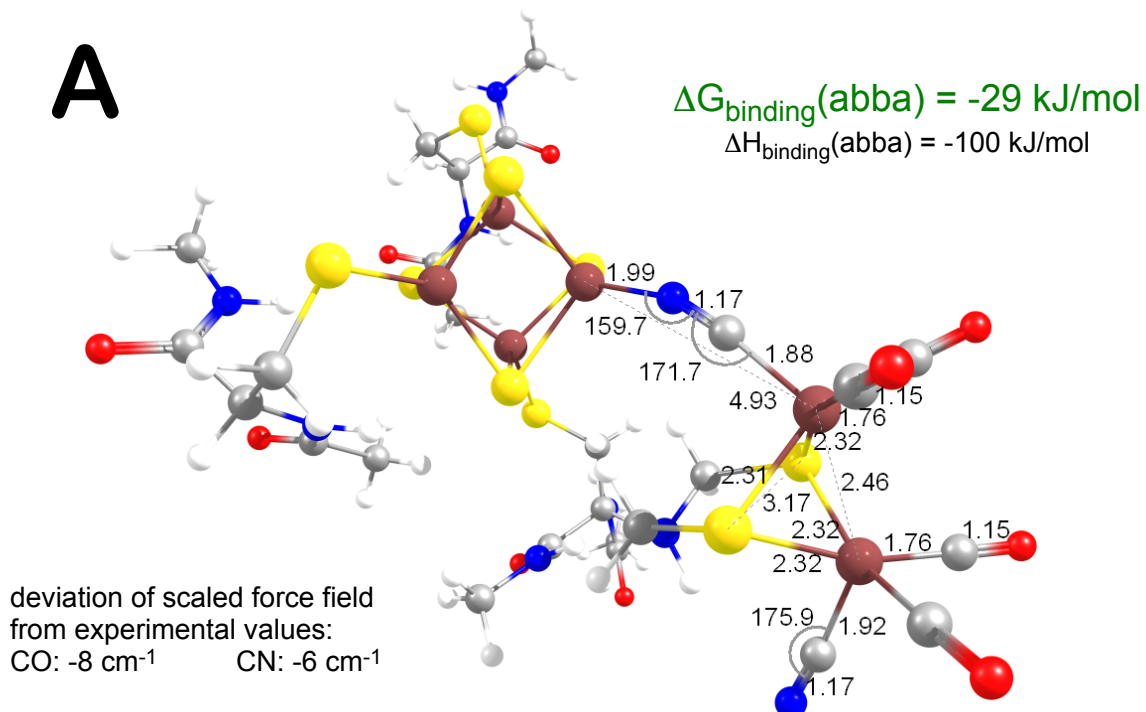
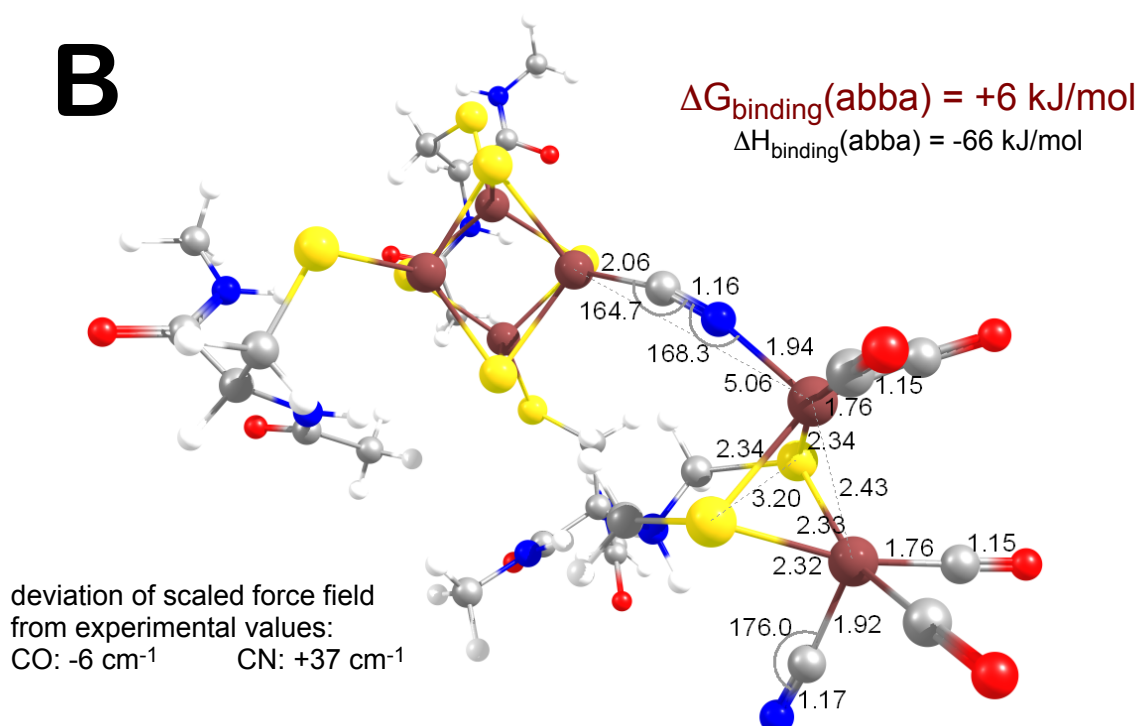
A**B**

Figure S12.8: Comparison of partially optimized *in proteo* models with constrained backbone atoms of **Model E** as derived from *TmeHydF* crystal structure with bridging apical cyanide coordination ($[4\text{Fe}-4\text{S}]^{2+} \times [\text{Fe}^{(\text{I})}\text{Fe}^{(\text{I})}]^{2-}$ open-shell singlet, spin polarized electronic state with total of 18 unpaired electrons, ‘abab’ spin coupling) calculated at $\omega\text{B97X-D/SVP}$ level.

References for supporting information

1. Caserta, G.; Pecqueur, L.; Adamska-Venkatesh, A.; Papini, C.; Roy, S.; Artero, V.; Atta, M.; Reijerse, E.; Lubitz, W.; Fontecave, M. *Nat. Chem. Biol.* **2017**, *13*, 779-784.
2. Li, H.; Rauchfuss, T. B. *J. Am. Chem. Soc.* **2002**, *124*, 726-727.
3. Le Cloirec, A.; C. Davies, S.; J. Evans, D.; L. Hughes, D.; J. Pickett, C.; P. Best, S.; Borg, S. *Chem. Comm.* **1999**, 2285-2286.
4. Schmidt, M.; Contakes, S. M.; Rauchfuss, T. B. *J. Am. Chem. Soc.* **1999**, *121*, 9736-9737.
5. Lyon, E. J.; Georgakaki, I. P.; Reibenspies, J. H.; Dahrenbourg, M. Y. *Angew. Chem. Int. Ed.* **1999**, *38*, 3178-3180.
6. Gloaguen, F.; Lawrence, J. D.; Schmidt, M.; Wilson, S. R.; Rauchfuss, T. B. *J. Am. Chem. Soc.* **2001**, *123*, 12518-12527.
7. Yu, L.; Greco, C.; Bruschi, M.; Ryde, U.; De Gioia, L.; Reiher, M. *Inorg. Chem.* **2011**, *50*, 3888-3900.
8. Tye, J. W.; Dahrenbourg, M. Y.; Hall, M. B. *J. Comp. Chem.* **2006**, *27*, 1454-1462.
9. Tye, J. W.; Dahrenbourg, M. Y.; Hall, M. B. *Inorg. Chem.* **2008**, *47*, 2380-2388.
10. Liaw, W.-F.; Tsai, W.-T.; Gau, H.-B.; Lee, C.-M.; Chou, S.-Y.; Chen, W.-Y.; Lee, G.-H. *Inorg. Chem.* **2003**, *42*, 2783-2788.
11. Stoll, S.; Schweiger, A. *J. Magn. Res.* **2006**, *178*, 42-55.
12. Shepard, E. M.; Byer, A. S.; Betz, J. N.; Peters, J. W.; Broderick, J. B. *Biochemistry* **2016**, *55*, 3514-3527.